

# Contents

<b>2</b>	<b>Phenomenology of sterile neutrinos</b>	<b>1</b>
2.1	Supernova neutrino experiments and the neutrino mass hierarchy . .	2
2.2	Short-baseline neutrino experiments and the number of neutrino species	11
2.3	Short-baseline neutrino experiments and leptonic CP-violation . . . .	28
2.3.1	Neutrino oscillation formalism . . . . .	29
2.3.2	Analysis method . . . . .	31
2.3.3	Results . . . . .	33
	<b>Bibliography</b>	<b>42</b>

# Chapter 2

## Phenomenology of sterile neutrinos

In this Chapter, the phenomenological work done over the past four years on sterile neutrinos is presented. The Chapter is divided into three sections:

- Section 2.1 discusses the constraints on sterile neutrino mass hierarchies, obtained from the observation of supernova neutrinos;
- Section 2.2 discusses the constraints on the number of light sterile neutrinos, their masses and their mixings, achieved from a combined analysis of accelerator-based and reactor-based short-baseline neutrino experiments;
- Section 2.3 discusses the constraints on leptonic CP-violation in (3+2) sterile neutrino models obtained from short-baseline neutrino experiments, and implications for the interpretation of the forthcoming MiniBooNE results on  $\nu_\mu \rightarrow \nu_e$  and (possibly)  $\bar{\nu}_\mu \rightarrow \bar{\nu}_e$  oscillations.

## 2.1 Supernova neutrino experiments and the neutrino mass hierarchy

The very dense matter environment traversed by supernova neutrinos affects how neutrinos are believed to oscillate among flavors: in this case, the neutrino mass hierarchy, that is the ordering of the neutrino mass eigenvalues, plays a role. Under certain approximations, it is possible to analytically derive the probability for muon and tau neutrinos produced in supernova explosions to be detected as electron neutrinos on Earth, as a function of the neutrino mass hierarchy and mixing parameters.

Detailed simulation models of the neutrino transport in core-collapse supernova explosions indicate different energy distributions for the electron, muon, and tau neutrino flavors at their surfaces of last scattering.

Electron neutrinos originated from the SN1987A supernova explosion that occurred in the neighbourhood of our galaxy have been observed on Earth. Therefore, the observation of the electron neutrino energy spectrum on Earth provides (model-dependent) constraints on muon/tau neutrino transitions to electron neutrinos, and therefore on the neutrino mass hierarchy and mixings.

The following paper (see Ref. [1] and references therein), written in collaboration with J. Conrad, discusses these constraints for various sterile neutrino models. The main result of the paper is that several sterile neutrino mass hierarchies are strongly disfavored, based on the SN1987A observations, providing an experimental way to constrain the large “phase space” of sterile neutrino models that are present in the literature.

# Supernova neutrinos and the LSND evidence for neutrino oscillations

Michel Sorel\* and Janet Conrad†

*Department of Physics, Columbia University, New York, New York 10027*

(Received 15 December 2001; published 23 August 2002)

The observation of the  $\bar{\nu}_e$  energy spectrum from a supernova burst can provide constraints on neutrino oscillations. We derive formulas for adiabatic oscillations of supernova antineutrinos for a variety of 3- and 4-neutrino mixing schemes and mass hierarchies which are consistent with the Liquid Scintillation Neutrino Detector (LSND) evidence for  $\bar{\nu}_\mu \rightarrow \bar{\nu}_e$  oscillations. Finally, we explore the constraints on these models and LSND given by the supernova SN 1987A  $\bar{\nu}_e$ 's observed by the Kamiokande-2 and IMB-3 detectors.

DOI: 10.1103/PhysRevD.66.033009

PACS number(s): 14.60.Pq, 14.60.St, 26.50.+x, 97.60.Bw

## I. INTRODUCTION

In recent years, the treatment of neutrino transport in the environment of a core-collapse supernova (SN) explosion has improved to the point of making realistic predictions on the observables for neutrinos reaching the Earth [1–4]. Of particular interest for this paper are the average energies at the neutrinospheres, i.e. the surfaces of last scattering for the neutrinos, estimated to be 10–13 MeV for  $\nu_e$ , 14–17 MeV for  $\bar{\nu}_e$ , 23–27 MeV for  $\nu_{\mu,\tau}$ ,  $\bar{\nu}_{\mu,\tau}$  [2,4].

The differences in temperatures between the various neutrino flavors can be qualitatively understood. Heavy-lepton neutrinos can interact only via neutral current (NC) processes, the main contribution to their transport opacity coming from neutrino-nucleon scattering, which dominates over neutrino-electron scattering. In addition to this same NC contribution, the transport opacity for  $\nu_e$ 's and  $\bar{\nu}_e$ 's depends also on the charged current (CC) absorptions  $\nu_e + n \rightarrow p + e^-$  and  $\bar{\nu}_e + p \rightarrow n + e^+$ , respectively. Therefore, the  $\nu_e$ - and  $\bar{\nu}_e$ -spheres are located at larger radii with respect to the other neutrinospheres, that is at lower densities and lower temperatures. Moreover, in a neutron-rich environment,  $\nu_e + n \rightarrow p + e^-$  dominates over  $\bar{\nu}_e + p \rightarrow n + e^+$ : the emergent  $\nu_e$ 's originate from layers farther outside the center of the star compared to  $\bar{\nu}_e$ 's, therefore at lower temperatures. The total energy released in a SN explosion is approximately equipartitioned between the different neutrino and antineutrino flavors [3].

The above predictions can be confronted with the observation of the supernova  $\bar{\nu}_e$  energy spectrum detected on Earth. Neutrino oscillations are expected to modify the spectrum since  $\langle E_{\bar{\nu}_e}^- \rangle < \langle E_{\bar{\nu}_\mu, \bar{\nu}_\tau}^- \rangle$ . The energy dependence of the neutrino cross section in the detector material, approximately  $\sigma_{\bar{\nu}_e p}^- \propto (E_{\bar{\nu}_e}^- - 1.29 \text{ MeV})^2$  [5], helps in making the  $\bar{\nu}_e$  energy spectrum distortion a sensitive experimental probe to neutrino oscillations. This is because higher energy neutrinos interact significantly more than lower energy ones.

We show that the extent of the spectrum modification depends crucially on the specifics of the neutrino mixing scheme and on the neutrino mass hierarchy under consideration, and we derive the relevant formulas assuming an adiabatic propagation for the antineutrinos in the supernova environment. Antineutrinos propagate adiabatically if the varying matter density they encounter changes slowly enough so that transitions between local (instantaneous) Hamiltonian eigenstates can be neglected throughout the entire antineutrino propagation. So far, neutrinos from one supernova have been detected and their energy measured: SN 1987A was observed by the Kamiokande-2 and IMB-3 detectors. The overall 20 events seen by those two detectors have all been interpreted as  $\bar{\nu}_e$  interactions [6]. We examine the constraint of such observations on the LSND allowed region of  $\bar{\nu}_\mu \rightarrow \bar{\nu}_e$  oscillations [7], for various neutrino mass and mixing models. If the LSND evidence is confirmed by the MiniBooNE experiment [8], several models can be excluded or constrained on the basis of the observations of the supernova SN 1987A and possibly future supernovæ.

## II. ADIABATIC OSCILLATIONS AND NEUTRINO MIXING SCHEMES

### A. $\bar{\nu}_e$ energy spectrum and the permutation factor

In the presence of neutrino oscillations, the  $\bar{\nu}_e$  flux reaching the Earth,  $F_{\bar{\nu}_e}^-$ , can be different from the primary flux at the neutrinosphere,  $F_{\bar{\nu}_e}^0$ . We will assume that, at production, the energy of active antineutrinos is equally divided into the three active flavors, i.e. that  $\int_0^\infty dE_{\bar{\nu}_\alpha}^- E_{\bar{\nu}_\alpha}^- F_{\bar{\nu}_\alpha}^0$  has the same numerical value for  $\alpha = e, \mu, \tau$ . Moreover, we will also consider neutrino mixing models where the three active neutrino species are augmented by a fourth sterile neutrino with no standard weak couplings: in those cases, we will assume that the sterile component is negligible at production.

The neutrino flux reaching the Earth is

$$F_{\bar{\nu}_e}^- = (p_{\mu \rightarrow e} + p_{\tau \rightarrow e}) F_{\bar{\nu}_\mu}^0 + p_{e \rightarrow e} F_{\bar{\nu}_e}^0 \\ \propto [p F_{\bar{\nu}_\mu}^0 + (1-p) F_{\bar{\nu}_e}^0] \quad (1)$$

where we have defined the *permutation factor*  $p$  as

\*Electronic address: sorel@fnal.gov

†Electronic address: conrad@fnal.gov

$$p = \frac{p_{\mu \rightarrow e} + p_{\tau \rightarrow e}}{p_{\mu \rightarrow e} + p_{\tau \rightarrow e} + p_{e \rightarrow e}} \quad (2)$$

and  $p_{\mu, \tau, e \rightarrow e}$  are the probabilities for a  $\bar{\nu}_\mu$ ,  $\bar{\nu}_\tau$ ,  $\bar{\nu}_e$  respectively at the neutrinosphere to oscillate into a  $\bar{\nu}_e$ . In Eqs. (1), (2), we have assumed that  $p$  is energy-independent (as will be justified later), and that  $\langle E_{\bar{\nu}_\mu}^- \rangle = \langle E_{\bar{\nu}_\tau}^- \rangle$ . In Eq. (1), we neglect the (energy-independent) proportionality factor since we will not deal with event rates, but only with neutrino energy distributions.

### B. Neutrino propagation in the adiabatic approximation

In vacuum, the Hamiltonian that governs neutrino propagation is diagonal in the mass eigenstate basis  $|\nu_i\rangle$ :

$$(H_0)_{ij} \equiv \langle \nu_i | H_0 | \nu_j \rangle = E_i \delta_{ij}. \quad (3)$$

If the neutrinos all have the same relativistic momentum  $p$ , their energies  $E_i$  differ only by a term proportional to their squared-mass differences, since  $E_i \approx p + m_i^2/2p$ . If  $U$  is the unitary mixing matrix that relates the flavor eigenstates  $|\nu_\alpha\rangle$  to the mass eigenstates via  $|\nu_\alpha\rangle = U_{\alpha i} |\nu_i\rangle$ , the elements of the vacuum Hamiltonian in the flavor basis are given by [9]:

$$(H_0)_{\alpha\beta} = U_{\alpha i}^* U_{\beta i} \frac{m_i^2}{2p} \quad (4)$$

where we have neglected the contribution  $p \delta_{\alpha\beta}$  in  $(H_0)_{\alpha\beta}$ , which is irrelevant for neutrino oscillations.

In matter,  $\bar{\nu}_e$ 's undergo coherent charged current (CC) forward-scattering from electrons, and all active flavor antineutrinos coherent neutral current (NC) forward-scattering from electrons, protons, and neutrons in the medium. These processes give rise to an interaction potential  $V = V_W + V_Z$ , which is diagonal in the flavor basis and proportional to the matter density  $\rho$ :

$$(V)_{\alpha\beta} = A_\alpha \frac{G_F \rho}{m_N} \delta_{\alpha\beta} \quad (5)$$

where  $A_\alpha$  is a proportionality constant, in general different for  $\alpha = e, \mu, \tau$ , or  $s$ ,  $G_F$  the Fermi constant, and  $m_N$  the nucleon mass. The relevant Hamiltonian for neutrino propagation in matter is therefore  $H \equiv H_0 + V$ .

At the neutrinosphere, the density  $\rho$  is so high ( $\sim 10^{12} \text{ g/cm}^3$  [1]) that the interaction potential dominates over the vacuum Hamiltonian, so that the propagation eigenstates coincide with the flavor eigenstates. As the propagation eigenstates free-stream outwards, toward regions of lower density, their flavor composition changes, ultimately reaching the flavor composition of the mass eigenstates in the vacuum. Given that the neutrinos escape the SN as mass eigenstates, no further flavor oscillations occur on their path to the Earth.

More specifically, making use of the adiabatic approximation and of the fact that no energy-level crossing is permitted, the flavor eigenstate at the neutrinosphere with the maximum interaction potential reaches Earth as the mass

TABLE I. Adiabatic neutrino propagation in the SN ejecta for the neutrino mixing models considered.

Model	Hierarchy	Propagation
Normal (1+1+1)	$m_3 > m_2 > m_1$	$\bar{\nu}_\gamma \rightarrow \bar{\nu}_3$ $\bar{\nu}_\beta \rightarrow \bar{\nu}_2$ $\bar{\nu}_\alpha \rightarrow \bar{\nu}_1$
Normal (1+1)	$m_2 \gg m_1$	$\bar{\nu}_\mu \rightarrow \bar{\nu}_2$ $\bar{\nu}_e \rightarrow \bar{\nu}_1$
LSND-inverted (1+1)	$m_1 \gg m_2$	$\bar{\nu}_\mu \rightarrow \bar{\nu}_1$ $\bar{\nu}_e \rightarrow \bar{\nu}_2$
Normal (2+1)	$m_3 > m_2 \gg m_1$	$\bar{\nu}_\mu \rightarrow \bar{\nu}_3$ $\bar{\nu}_\tau \rightarrow \bar{\nu}_2$ $\bar{\nu}_e \rightarrow \bar{\nu}_1$
LSND-inverted (2+1)	$m_1 \gg m_3 > m_2$	$\bar{\nu}_\mu \rightarrow \bar{\nu}_1$ $\bar{\nu}_\tau \rightarrow \bar{\nu}_3$ $\bar{\nu}_e \rightarrow \bar{\nu}_2$
Normal (2+2)	$m_3 > m_2 \gg m_1 > m_0$	$\bar{\nu}_\mu \rightarrow \bar{\nu}_3$ $\bar{\nu}_\tau \rightarrow \bar{\nu}_2$ $\bar{\nu}_s \rightarrow \bar{\nu}_1$ $\bar{\nu}_e \rightarrow \bar{\nu}_0$
LSND-inverted (2+2)	$m_1 > m_0 \gg m_3 > m_2$	$\bar{\nu}_\mu \rightarrow \bar{\nu}_1$ $\bar{\nu}_\tau \rightarrow \bar{\nu}_0$ $\bar{\nu}_s \rightarrow \bar{\nu}_3$ $\bar{\nu}_e \rightarrow \bar{\nu}_2$
Normal (3+1)	$m_4 \gg m_3 > m_2 > m_1$	$\bar{\nu}_\mu \rightarrow \bar{\nu}_4$ $\bar{\nu}_\tau \rightarrow \bar{\nu}_3$ $\bar{\nu}_s \rightarrow \bar{\nu}_2$ $\bar{\nu}_e \rightarrow \bar{\nu}_1$
LSND-inverted (3+1)	$m_3 > m_2 > m_1 \gg m_4$	$\bar{\nu}_\mu \rightarrow \bar{\nu}_3$ $\bar{\nu}_\tau \rightarrow \bar{\nu}_2$ $\bar{\nu}_s \rightarrow \bar{\nu}_1$ $\bar{\nu}_e \rightarrow \bar{\nu}_4$

eigenstate with the biggest neutrino mass. In general, the energy level order is maintained throughout the neutrino propagation in the SN ejecta. This is illustrated in Table I for three neutrinos in the row labeled “normal (1+1+1),” where we have taken  $A_\gamma > A_\beta > A_\alpha$  and  $m_3 > m_2 > m_1$ .

For example, the probability for a  $\bar{\nu}_\alpha$  to emerge from the SN environment as a  $\bar{\nu}_\beta$  is given by

$$p_{\alpha \rightarrow \beta} = |\langle \bar{\nu}_\beta | U^{evol} | \bar{\nu}_\alpha \rangle|^2 = |\langle U_{\beta i} \bar{\nu}_i | U^{evol} | \bar{\nu}_\alpha \rangle|^2 \\ = |U_{\beta i}^* \delta_{i,1}|^2 = |U_{\beta 1}|^2 \quad (6)$$

where  $U^{evol}$  is the adiabatic evolution operator. In Eq. (6), we have used Table I to get

$$\langle \bar{\nu}_i | U^{evol} | \bar{\nu}_\alpha \rangle = \delta_{i,1}. \quad (7)$$

TABLE II. Results on the probabilities  $p_{\mu,\tau,e \rightarrow e}$  for a  $\bar{\nu}_{\mu,\tau,e}$  to emerge from the SN as a  $\bar{\nu}_e$ , the permutation factor  $p$  of Eq. 2, and the LSND oscillation amplitude  $\sin^2 2\vartheta_{\text{LSND}}$ , for the various neutrino mixing schemes considered.

Model	Mixing	$p_{\mu \rightarrow e}$	$p_{\tau \rightarrow e}$	$p_{e \rightarrow e}$	$p$	$\sin^2 2\vartheta_{\text{LSND}}$
Normal (1+1)	Eq. (10)	$\sin^2 \vartheta$	0	$\cos^2 \vartheta$	$\sin^2 \vartheta$	$\sin^2 2\vartheta = 4p(1-p)$
LSND-inverted (1+1)	Eq. (10)	$\cos^2 \vartheta$	0	$\sin^2 \vartheta$	$\cos^2 \vartheta$	$\sin^2 2\vartheta = 4p(1-p)$
Normal (2+1)	Eq. (11)	$\frac{3}{4}\alpha^2$	$\frac{1}{4}\alpha^2$	1	$\alpha^2/(1+\alpha^2)$	$4\alpha^2 = 4p/(1-p)$
LSND-inverted (2+1)	Eq. (11)	1	$\frac{3}{4}\alpha^2$	$\frac{1}{4}\alpha^2$	$(1+\frac{3}{4}\alpha^2)/(1+\alpha^2)$	$4\alpha^2 = 4(1-p)/(p-\frac{3}{4})$
Normal (2+2)	Eq. (14)	$\beta^2$	$\beta^2$	$\frac{1}{2}$	$4\beta^2/(1+4\beta^2)$	$8\beta^2 = 2p/(1-p)$
LSND-inverted (2+2)	Eq. (14)	$\frac{1}{2}$	$\frac{1}{2}$	$\beta^2$	$1/(1+\beta^2)$	$8\beta^2 = 8(1-p)/p$
Normal (3+1)	Eq. (15)	$\gamma^2$	0	$\frac{1}{2}$	$2\gamma^2/(1+2\gamma^2)$	$4\gamma^2\delta^2 = 2\delta^2 p/(1-p)$
LSND-inverted (3+1)	Eq. (15)	0	$\frac{1}{2}$	$\gamma^2$	$1/(1+2\gamma^2)$	$4\gamma^2\delta^2 = 2\delta^2(1-p)/p$

This result can be immediately generalized to any number of antineutrino generations. Also, as long as the adiabatic approximation is satisfied, the formula does not depend on the specific dynamics for the neutrino propagation, for example on the number and position in the SN environment of Mikheyev-Smirnov-Wolfenstein (MSW) resonances. We will comment more on the validity of the adiabatic approximation in the next section.

In this paper, we consider three or four flavor components, including a sterile one. At tree-level, the proportionality factors  $A_\alpha$  in the interaction potential for neutral matter are [9,10]

$$A = \begin{cases} (1-3Y_e)/\sqrt{2} & \text{for } \bar{\nu}_e, \\ (1-Y_e)/\sqrt{2} & \text{for } \bar{\nu}_\mu, \bar{\nu}_\tau, \\ 0 & \text{for } \bar{\nu}_s, \end{cases} \quad (8)$$

where  $Y_e$  is the electron fraction per nucleon. Following the assumptions of [10,11], we use  $Y_e \approx (1 + \langle E_{\bar{\nu}_e} \rangle / \langle E_{\nu_e} \rangle)^{-1} > 1/3$  at the neutrinosphere. Considering also one-loop electroweak radiative corrections, a difference in the  $\bar{\nu}_\mu$  and  $\bar{\nu}_\tau$  interaction potentials of magnitude  $(A_\mu - A_\tau)/A_\mu \sim 10^{-4}$  appears due to the difference in the charged lepton masses [12,13]. At the neutrinosphere, this second-order effect in the interaction potential dominates over the vacuum Hamiltonian terms (as long as  $|m_i^2 - m_j^2| < 10 \text{ eV}^2$  for all  $i, j$ ), and removes the  $\bar{\nu}_\mu - \bar{\nu}_\tau$  degeneracy. Therefore, for the antineutrino channel considered here, we take

$$A_\mu > A_\tau > A_s > A_e. \quad (9)$$

For the neutrino channel, one should substitute  $A \rightarrow -A$  in Eq. (8), and the order in Eq. (9) would be inverted.

Therefore, given a specific neutrino mass and mixing model, the permutation factor can be easily evaluated in the adiabatic approximation, and its numerical value does not depend on the neutrino energy. We will comment on possible energy-dependent Earth matter effects in the next section. In practice, one proceeds backwards: given a certain measured value of  $p$ , it is possible to constrain possible models for neutrino oscillations. This approach is used for example in

[13] to constrain models explaining the solar and atmospheric neutrino data; in this paper, we focus on 3 and 4-neutrino models explaining the Liquid Scintillation Neutrino Detector (LSND) data.

### C. Possible mixing schemes

The results for the  $\bar{\nu}_\mu, \bar{\nu}_\tau, \bar{\nu}_e \rightarrow \bar{\nu}_e$  adiabatic oscillation probabilities, the permutation factor  $p$ , and the LSND oscillation amplitude  $\sin^2 2\vartheta$  as a function of the mixing parameters and  $p$  for the eight possible mass and mixing schemes considered below are given in Table II. The mass hierarchy and the adiabatic propagation of the neutrino eigenstates for these mixing schemes are depicted in Table I.

The simplest possible mixing scheme is a (1+1) model explaining only  $\bar{\nu}_\mu \rightarrow \bar{\nu}_e$  LSND oscillations in vacuum, and not the atmospheric or solar oscillations:

$$\begin{pmatrix} \bar{\nu}_e \\ \bar{\nu}_\mu \end{pmatrix} = \begin{pmatrix} \cos \vartheta & \sin \vartheta \\ -\sin \vartheta & \cos \vartheta \end{pmatrix} \begin{pmatrix} \bar{\nu}_1 \\ \bar{\nu}_2 \end{pmatrix}, \quad (10)$$

where the mixing angle  $\vartheta$  can assume any value in the range  $0 < \vartheta < \pi/4$ .

We consider a (2+1) model motivated, for example, by *CPT*-violating scenarios (see, e.g. [14]), in which atmospheric and LSND oscillations in the antineutrino channel are obtained via the mixing [15]:

$$\begin{pmatrix} \bar{\nu}_e \\ \bar{\nu}_\mu \\ \bar{\nu}_\tau \end{pmatrix} = \begin{pmatrix} 1 & -\frac{1}{2}\alpha & -\frac{\sqrt{3}}{2}\alpha \\ \alpha & \frac{1}{2} & \frac{\sqrt{3}}{2} \\ 0 & -\frac{\sqrt{3}}{2} & \frac{1}{2} \end{pmatrix} \begin{pmatrix} \bar{\nu}_1 \\ \bar{\nu}_2 \\ \bar{\nu}_3 \end{pmatrix}. \quad (11)$$

The matrix in Eq. (11) is chosen to ensure large  $\bar{\nu}_\mu \rightarrow \bar{\nu}_\tau$  mixing for atmospheric neutrinos ( $\sin^2 2\vartheta_{\text{atm}} = 3/4$ ), while the LSND  $\bar{\nu}_\mu \rightarrow \bar{\nu}_e$  mixing is fixed by the parameter  $\alpha$  ( $\sin^2 2\vartheta_{\text{LSND}} = 4\alpha^2$ ).

The most popular models which explain the solar, atmospheric and LSND signatures (and the null results obtained

by other experiments) via neutrino oscillations invoke the existence of a sterile neutrino  $\bar{\nu}_s$ . One example of a (2 + 2) model is the following, which is taken from [16]:

$$\begin{pmatrix} \bar{\nu}_s \\ \bar{\nu}_e \\ \bar{\nu}_\mu \\ \bar{\nu}_\tau \end{pmatrix} = \begin{pmatrix} \frac{1}{\sqrt{2}} & \frac{1}{\sqrt{2}} & 0 & 0 \\ -\frac{1}{\sqrt{2}} & \frac{1}{\sqrt{2}} & \beta & \beta \\ \beta & -\beta & \frac{1}{\sqrt{2}} & \frac{1}{\sqrt{2}} \\ 0 & 0 & -\frac{1}{\sqrt{2}} & \frac{1}{\sqrt{2}} \end{pmatrix} \begin{pmatrix} \bar{\nu}_0 \\ \bar{\nu}_1 \\ \bar{\nu}_2 \\ \bar{\nu}_3 \end{pmatrix} \quad (12)$$

where one pair of nearly degenerate mass eigenstates has maximal  $\nu_e \rightarrow \nu_s$  mixing for solar neutrinos and the other pair has maximal  $\nu_\mu \rightarrow \nu_\tau$  mixing for atmospheric neutrinos. Small inter-doublet mixings through the  $\beta$  parameter accommodate the LSND result ( $\sin^2 \vartheta_{\text{LSND}} = 8\beta^2$ ).

Recent experimental results [17] show that pure  $\nu_e \rightarrow \nu_s$  solar oscillations are excluded at high significance. We therefore consider a more general (2 + 2) scenario, in which solar neutrinos can undergo any combination of  $\nu_e \rightarrow \nu_s$  and  $\nu_e \rightarrow \nu_\tau$  oscillations, while atmospheric neutrinos can undergo any combination of  $\nu_\mu \rightarrow \nu_\tau$  and  $\nu_\mu \rightarrow \nu_s$  oscillations. We follow the procedure in [18] to obtain this more general mixing starting from Eq. (12), by substituting the  $(\bar{\nu}_s, \bar{\nu}_\tau)$  states with the rotated states  $(\bar{\nu}'_s, \bar{\nu}'_\tau)$ :

$$\begin{pmatrix} \bar{\nu}'_s \\ \bar{\nu}'_\tau \end{pmatrix} = \begin{pmatrix} \cos \varphi_s & \sin \varphi_s \\ -\sin \varphi_s & \cos \varphi_s \end{pmatrix} \begin{pmatrix} \bar{\nu}_s \\ \bar{\nu}_\tau \end{pmatrix} \quad (13)$$

where the rotation angle  $\varphi_s$  fixes the sterile component in the atmospheric doublet ( $0 < \varphi_s < \pi/2$ ). Equation (12) then becomes

$$\begin{pmatrix} \bar{\nu}_s \\ \bar{\nu}_e \\ \bar{\nu}_\mu \\ \bar{\nu}_\tau \end{pmatrix} = \begin{pmatrix} \frac{\cos \varphi_s}{\sqrt{2}} & \frac{\cos \varphi_s}{\sqrt{2}} & \frac{\sin \varphi_s}{\sqrt{2}} & -\frac{\sin \varphi_s}{\sqrt{2}} \\ -\frac{1}{\sqrt{2}} & \frac{1}{\sqrt{2}} & \beta & \beta \\ \beta & -\beta & \frac{1}{\sqrt{2}} & \frac{1}{\sqrt{2}} \\ \frac{\sin \varphi_s}{\sqrt{2}} & \frac{\sin \varphi_s}{\sqrt{2}} & -\frac{\cos \varphi_s}{\sqrt{2}} & \frac{\cos \varphi_s}{\sqrt{2}} \end{pmatrix} \begin{pmatrix} \bar{\nu}_0 \\ \bar{\nu}_1 \\ \bar{\nu}_2 \\ \bar{\nu}_3 \end{pmatrix} \quad (14)$$

which contains Eq. (12) in the specific case  $\varphi_s = 0$ . We note that the LSND oscillation amplitude formula  $\sin^2 \vartheta_{\text{LSND}} = 8\beta^2$  holds also for the more general case of Eq. (14), and that our results are independent of the value of  $\varphi_s$  (see Table II).

Another possible 4-neutrino model has a (3 + 1) hierarchy; as an example for this model, here we consider the following mixing, which is also taken from [16]:

$$\begin{pmatrix} \bar{\nu}_e \\ \bar{\nu}_\mu \\ \bar{\nu}_\tau \\ \bar{\nu}_s \end{pmatrix} = \begin{pmatrix} \frac{1}{\sqrt{2}} & \frac{1}{\sqrt{2}} & 0 & \gamma \\ -\frac{1}{2} & \frac{1}{2} & \frac{1}{\sqrt{2}} & \delta \\ \frac{1}{2} & -\frac{1}{2} & \frac{1}{\sqrt{2}} & 0 \\ \frac{1}{2}\delta - \frac{1}{\sqrt{2}}\gamma & -\frac{1}{2}\delta - \frac{1}{\sqrt{2}}\gamma & -\frac{1}{\sqrt{2}}\delta & 1 \end{pmatrix} \begin{pmatrix} \bar{\nu}_1 \\ \bar{\nu}_2 \\ \bar{\nu}_3 \\ \bar{\nu}_4 \end{pmatrix} \quad (15)$$

where the solar and atmospheric oscillations are approximately described by oscillations of three active neutrinos, and the LSND result by a coupling of  $\bar{\nu}_\mu$  and  $\bar{\nu}_e$  through small mixings with  $\bar{\nu}_s$  that has a mass eigenvalue widely separated from the others ( $\sin^2 \vartheta_{\text{LSND}} = 4\gamma^2\delta^2$ ). For the (3 + 1) scenario, the constraint given by the permutation probability  $p$  is not sufficient to determine the LSND oscillation amplitude  $\sin^2 \vartheta_{\text{LSND}}$ . Therefore, the constraint on  $|U_{\mu 4}|^2 = \delta^2$  given by the CDHS and Super-K experiments will also be used, as explained later.

We should note that the mixing matrices defined in Eqs. (10)–(15) are approximations in the sense that the matrices are unitary only up to order  $\mathcal{O}(\alpha, \beta, \gamma, \delta)$ . These are the parameters in the mixings responsible for LSND-type oscillations, which we let float for our analysis, but we know they are small.

In order to determine the permutation factor for the mixing models, we also need to specify the neutrino mass hierarchy. In this paper, we consider for each mixing model both the cases of “normal” and “LSND-inverted” mass hierarchies. By “normal” hierarchy, here we mean that  $m_i > m_j$  for  $i > j$ , where  $m_i$  is the mass eigenvalue for the  $|\bar{\nu}_i\rangle$  state. We define the “LSND-inverted” hierarchies as the ones obtained substituting  $\Delta m_{\text{LSND}} \rightarrow -\Delta m_{\text{LSND}}$  in the normal hierarchies, without changing the hierarchy of the eventual solar and atmospheric splittings (see Table I);  $\Delta m_{\text{LSND}}$  is the neutrino mass difference responsible for LSND oscillations.

A common feature to all the mixing schemes is apparent in Table II. In the adiabatic approximation, normal mass hierarchies predict small permutation factors, while an almost complete permutation would be present for LSND-inverted hierarchies.

Given the specific neutrino mixing models considered here, we can now partially address the question whether the adiabatic approximation is applicable in this context. At a



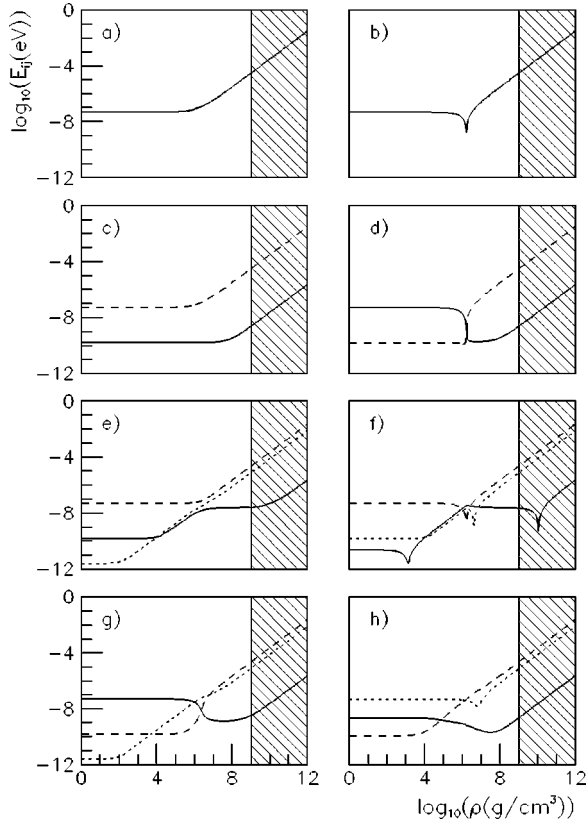


FIG. 1. Splittings between energy eigenvalues versus matter density  $\rho$  for various neutrino mass and mixing models. Solid, dashed, dotted lines show the splittings  $E_{12}$ ,  $E_{23}$ ,  $E_{34}$ , respectively (see text). The local minima correspond to MSW-resonances. Model (a) normal (1+1); (b) inverted (1+1); (c) normal (2+1); (d) inverted (2+1); (e) normal (2+2); (f) inverted (2+2); (g) normal (3+1); (h) inverted (3+1). Apart from the inconsequential  $\bar{\nu}_\mu \leftrightarrow \bar{\nu}_\tau$  one in (f), no MSW-resonances occur before the antineutrinos reach the stalled shock-wave (hatched area).

resonance, where the nonadiabaticity is maximal, this is a good approximation if the width of the resonance region is large compared with the local neutrino oscillation length. The width of the resonance is, in turn, determined by the characteristic length scale of the radial matter density variations at the resonance. While there are reliable models for the matter density profile of the progenitor star, there are still uncertainties on the profile seen by neutrinos in their free-streaming propagation.

It is now thought that neutrino heating of the proto-neutron star mantle drives the supernova explosion, which would happen with a  $\sim 1$  s delay after the creation of the shock-wave, ultimately responsible for the explosion; during this delay, the shock-wave would be stalled at a radius of  $\sim 200$  km from the neutron star, corresponding to a density  $\rho \sim 10^9 - 10^{10}$  g/cm<sup>3</sup> [1]. Therefore, the density profile in the proximity of the stalled shock-wave, which is difficult to model reliably, is a potential site for nonadiabatic oscillations.

In Fig. 1 we show the energy splittings between the local neutrino energy eigenvalues  $E_i$ , as a function of matter density, for all eight neutrino models considered here. For an

$n$ -neutrino model, we plot  $E_{i,i+1} \equiv E_i - E_{i+1}$ , where  $i = 1, \dots, n-1$ ; the eigenvalues are ordered such that  $E_1 > E_2 > \dots > E_n$ . Clearly, a resonance corresponds to a local minimum in one of the curves. As can be seen from Fig. 1, all the resonances [except the inconsequential one in Fig. 1(f) between  $\bar{\nu}_\mu$  and  $\bar{\nu}_\tau$  [19]] lie at densities well below the stalled shock-wave density of  $\rho \sim 10^9 - 10^{10}$  g/cm<sup>3</sup>. Therefore, the impact of level crossing between propagation eigenstates is likely to be small even where the neutrinos encounter the shock-wave.

If the SN neutrinos cross the Earth on their way to the detector, as for example happened for the SN 1987A  $\bar{\nu}_e$ 's detected by the Kamiokande-2 and IMB-3 detectors, it is also necessary to evaluate the importance of Earth matter effects in the neutrino propagation. Clearly, for neutrino oscillation models where no solar splitting is involved [for example the (1+1) and (2+1) models in this paper], this effect is negligible. In the models where such a splitting is allowed [i.e. the (2+2) and (3+1) models considered here], the situation is more complicated. However, the Earth matter effects have been shown to be small in this case as well for a large fraction of the SN  $\bar{\nu}_e$  energy spectrum (below  $\approx 40$  MeV) [13,20], and for the sake of simplicity will not be considered further.

### III. CONSTRAINTS ON LSND FROM SN 1987A OBSERVATIONS

Twenty  $\bar{\nu}_e$  events from the supernova SN 1987A were observed by the Kamiokande-2 (Kam-2) and IMB-3 detectors. Kam-2 saw 12 events with an average energy of  $\langle E_{det} \rangle = 14.7$  MeV, IMB-3 (which had a higher energy threshold than Kam-2) detected 8 events with  $\langle E_{det} \rangle = 31.9$  MeV [21].

From a comparison of the measured energy spectra ( $F_{\bar{\nu}_e}^-$ ) with theoretical models of neutrino emission ( $F_{\bar{\nu}_e}^0$  and  $F_{\bar{\nu}_\mu}^0$ ), it is possible to infer the permutation factor  $p$  in Eq. (1). SN 1987A observations are consistent with no-oscillations (i.e.  $p=0$ ). In Appendix A, we derive a conservative upper bound on  $p$  of  $p < 0.22$  at 99% C.L., by applying a Kholmogorov-Smirnov test on the joint Kam-IMB dataset and a range of supernova neutrino emission models.

One important result of our analysis is immediately apparent from the values of the permutation factors  $p$  as a function of the mixing parameters in Table II, and from the fact that the value of  $p$  inferred from SN 1987A data has to be less than 0.22 at 99% C.L. The four mixing schemes considered, explaining the LSND effect via a LSND-inverted neutrino mass hierarchy, are all incompatible with SN 1987A data.

We now consider the normal hierarchy cases. For the (1+1), (2+1) and (2+2) models with the mixings of Eqs. (10)–(12), the bound on the permutation factor  $p$  unambiguously determines the constraint on the LSND oscillation amplitude  $\sin^2 2\vartheta_{LSND}$  (see Table II). At 99% C.L., SN 1987A data provide no constraints on the (2+1) model, and a constraint which is weaker than existing bounds from the accel-



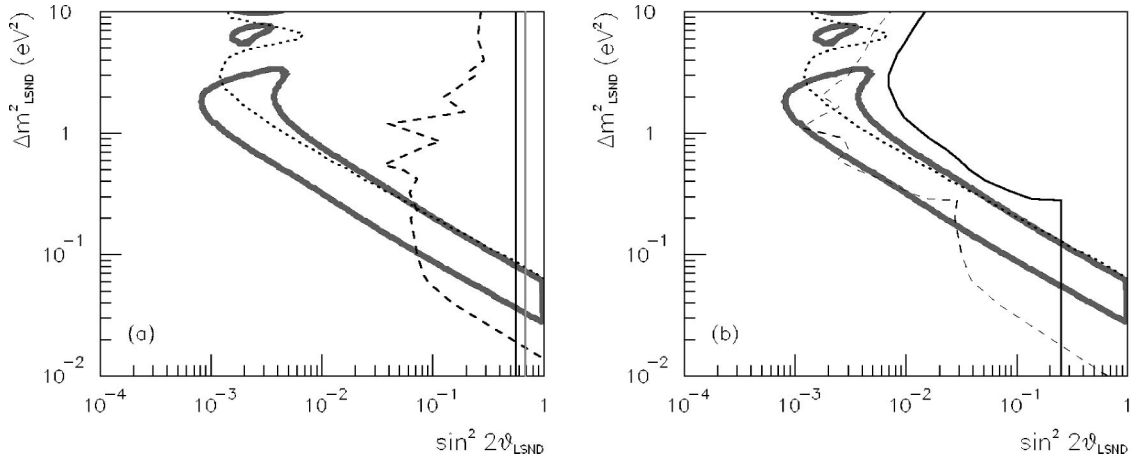


FIG. 2. 99% C.L. LSND allowed region [7] and 99% C.L. exclusion regions for the neutrino mixing schemes considered in the text and with normal mass hierarchy. The exclusion regions are estimated as in [26]. (a) shows the exclusion regions for the (1+1), (2+1) and (2+2) models, (b) for the (3+1) model. The exclusion regions refer to experimental data from the following experiments. (a) Dotted line: KARMEN; dashed line: Bugey; dark solid line: SN 1987A for the (2+2) model; light solid line: SN 1987 for the (1+1) model; SN 1987A data provide no constraints at 99% C.L. for the (2+1) model. (b) Dotted line: KARMEN; dashed line: Bugey, CDHS and Super-K; solid line: SN 1987A, CDHS and Super-K.

erator experiment KARMEN [23] and the reactor experiment Bugey [24,25] for the (1+1) and (2+2) models [see Fig. 2(a)]. Therefore, these models are compatible with the SN 1987A data.

As already mentioned, for the (3+1) model, the permutation factor does not fully determine the LSND oscillation amplitude:  $\sin^2 2\theta_{\text{LSND}}$  depends not only on  $p$ , but also on  $|U_{\mu 4}|^2 = \delta^2$ . Here we use the  $\Delta m_{\text{LSND}}^2$ -dependent constraints on  $\delta^2$  from the  $\nu_\mu$ -disappearance experiments CDHS (for  $\Delta m_{\text{LSND}}^2 > 0.3 \text{ eV}^2$ ) and Super-K (for  $\Delta m_{\text{LSND}}^2 < 0.3 \text{ eV}^2$ ) [25]. Moreover, another complication arises in evaluating exclusion regions for (3+1) models: given the 99% C.L. upper bounds on  $\gamma^2 = |U_{e4}|^2$  from SN 1987A and  $\delta^2 = |U_{\mu 4}|^2$  from CDHS and Super-K, what is the 99% C.L. upper bound on  $\sin^2 2\theta_{\text{LSND}} = 4\gamma^2\delta^2$ ? We follow the method described in [26] to estimate this bound. The same method is applied to estimate the 99% C.L. upper limit on  $\sin^2 2\theta_{\text{LSND}}$  coming from Bugey (for  $\gamma^2$ ) and CDHS and Super-K (for  $\delta^2$ ), that is without using the SN 1987A data. The results for the (3+1) model with normal neutrino mass hierarchy and mixing given by Eq. (15) are shown in Fig. 2(b). Also for this model, we find that existing constraints (the Bugey constraint on  $\delta^2$ , in this case) are stronger than the SN 1987A one.

Table III summarizes the SN 1987A constraints obtained in this paper on the LSND allowed region, for the various neutrino mass and mixing models considered.

#### IV. CONCLUSIONS

We have investigated the effect that 3- and 4-neutrino oscillation schemes would have in modifying the energy spectrum of supernova  $\bar{\nu}_e$ 's. Throughout the paper, we apply the adiabatic approximation for the antineutrino propagation in the supernova environment and neglect Earth matter effects. Moreover, we have used our results to test the compat-

ibility between the SN 1987A data and the LSND evidence for  $\bar{\nu}_\mu \rightarrow \bar{\nu}_e$  oscillations.

We have provided specific relations for the permutation factor, which gives the admixture of a higher energy flux to the original  $\bar{\nu}_e$  flux at production from  $\bar{\nu}_\mu, \bar{\nu}_\tau \rightarrow \bar{\nu}_e$  oscillations, for various neutrino mass and mixing models. The permutation factor may be measurable with good accuracy in future supernova experiments.

Based on SN 1987A data only, which seem to indicate a small (if nonzero) value for the permutation factor, we are able to exclude all of the four models considered which would explain the LSND signal via a “LSND-inverted” neutrino mass hierarchy, as defined in the text. For the normal mass hierarchy schemes considered, SN 1987A data do not provide any stronger constraints on the LSND allowed region for oscillations than those already obtained with reactor, accelerator and atmospheric neutrinos; additional experimental input is necessary to unambiguously discern the neutrino mass and mixing properties. Undoubtedly, the detection of

TABLE III. Summary of the SN 1987A constraints on the LSND allowed region, for the various models considered in this paper; see Fig. 2 also.

Model	SN 1987A constraint on LSND region (99% C.L.)
Normal (1+1)	partially excluded [Fig. 2(a)]
LSND-inverted (1+1)	excluded
Normal (2+1)	unconstrained
LSND-inverted (2+1)	excluded
Normal (2+2)	partially excluded [Fig. 2(a)]
LSND-inverted (2+2)	excluded
Normal (3+1)	partially excluded [Fig. 2(b)]
LSND-inverted (3+1)	excluded

supernova neutrinos by present or near-term experiments [27] would prove very useful in this respect.

### ACKNOWLEDGMENTS

We thank Kevork Abazajian, Vernon Barger, John Beacom, Nicole Bell, Steve Brice, Klaus Eitel, Lam Hui, Hitoshi Murayama and Michael Shaevitz for valuable discussions and useful suggestions. This work was supported by NSF and by the Sloan Foundation.

### APPENDIX: UPPER BOUNDS ON THE PERMUTATION FACTOR FROM SN 1987A DATA

In this appendix, we discuss the statistical methodology and the physics assumptions used to estimate the upper bound on the permutation factor  $p$  quoted in the text,  $p < 0.22$  at 99% C.L. We use the same statistical methodology as in [22], that is we use the Kholmogorov-Smirnov test on the joint Kam-IMB dataset to derive the upper bound. Most of the physics assumptions are identical to those in [28].

The expected energy spectrum for the positrons, observed in the Kamiokande and IMB detectors via the reaction  $\bar{\nu}_e p \rightarrow e^+ n$ , is

$$n_i(E_{det}) = \frac{N_{p,i}}{4\pi D^2} \int_0^\infty dE_+ P_i(E_{det}, E_+) \times \eta_{0,i}(E_+) \sigma_{\bar{\nu}_e p}(E_+ + Q) F_{\bar{\nu}_e}^0(E_+ + Q) \quad (A1)$$

where  $i$  refers to either Kam or IMB,  $N_{p,i}$  is the number of target protons in the detectors,  $D$  the distance between the Large Magellanic Cloud and the Earth,  $E_{det}(E_+)$  is the detected (true) positron energy,  $Q \equiv m_n - m_p = 1.29$  MeV  $\approx E_{\bar{\nu}_e} - E_+$ ,  $P_i(E_{det}, E_+)$ , and  $\eta_{0,i}(E_+)$  the energy resolution functions and efficiency curves taken from [28],  $\sigma_{\bar{\nu}_e p}(E_+ + Q) \propto E_+^2$  the neutrino interaction cross section taken from [5] (neglecting nuclear recoil), and finally  $F_{\bar{\nu}_e}^0(E_+ + Q)$  the neutrino flux at the detector taken from Eq. (1). We assume “unpinched” Fermi-Dirac distributions for the fluxes  $F_{\bar{\nu}_\alpha}^0$ ,  $\alpha = e, \mu$ , appearing in Eq. (1):

$$F_{\bar{\nu}_\alpha}^0(E) \propto \frac{E^2}{\langle E_{\bar{\nu}_\alpha}^- \rangle T_\alpha^3 (e^{E/T_\alpha} + 1)} \quad (A2)$$

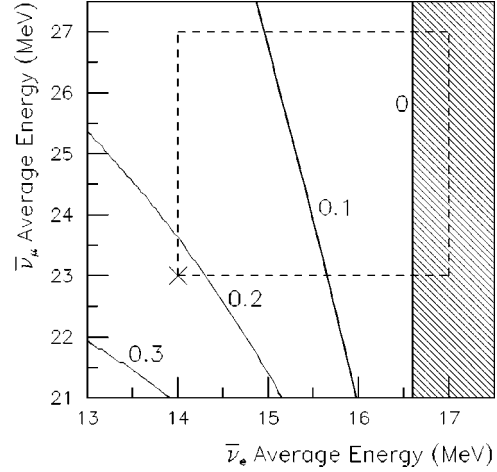


FIG. 3. Solid lines: isocontours for the upper bounds on the permutation factor  $p$  at 99% C.L. obtained from SN 1987A data, as a function of the  $\bar{\nu}_e$  and  $\bar{\nu}_\mu$  average energies predicted at production by supernova models; rectangle with dashed border: range of energies allowed by present models; cross: model chosen to derive the (conservative) upper bound on  $p$  used in the text. The region  $\langle E_{\bar{\nu}_e}^- \rangle > 16.6$  MeV is excluded at 99% C.L. for all values of  $p$ .

where  $\langle E_{\bar{\nu}_\alpha}^- \rangle \approx 3.15 T_\alpha$  at the denominator ensures energy equipartition.

The cumulative distribution function used for the Kholmogorov-Smirnov test is

$$\mathcal{F}(E_{det}) = \int_0^{E_{det}} dE [n_{Kam}(E) + n_{IMB}(E)]. \quad (A3)$$

Figure 3 shows the upper bound on the permutation factor  $p$  obtained from SN 1987A data, at 99% C.L., as a function of the average energies  $\langle E_{\bar{\nu}_e}^- \rangle$ ,  $\langle E_{\bar{\nu}_\mu}^- \rangle$ . As expected, the bound becomes more stringent for supernova models in which the neutrino average energies are higher. SN 1987A data are incompatible at 99% C.L. with all supernova neutrino models predicting  $\langle E_{\bar{\nu}_e}^- \rangle > 16.6$  MeV, for all values of  $p$  and  $\langle E_{\bar{\nu}_\mu}^- \rangle$ . We adopt a conservative approach, and quote as the upper bound on  $p$  the largest value for supernova neutrino models in the range  $14 < \langle E_{\bar{\nu}_e}^- \rangle < 17$  MeV,  $23 < \langle E_{\bar{\nu}_\mu}^- \rangle < 27$  MeV, that is the one corresponding to  $\langle E_{\bar{\nu}_e}^- \rangle = 14$  MeV,  $\langle E_{\bar{\nu}_\mu}^- \rangle = 23$  MeV (cross in Fig. 3).

- [1] A. Burrows *et al.*, *Astrophys. J.* **539**, 865 (2000).
- [2] H.-T. Janka, in *Proceedings of the Vulcano Workshop 1992, Frontier objects in astrophysics and particle physics*, pp. 345–374.
- [3] H.-T. Janka, *Astropart. Phys.* **3**, 377 (1995).
- [4] G.G. Raffelt, *Nucl. Phys. B (Proc. Suppl.)* **110**, 254 (2002).
- [5] P. Vogel and J.F. Beacom, *Phys. Rev. D* **60**, 053003 (1999).
- [6] There has been some discussion whether to interpret the first

Kam-2 event as  $\bar{\nu}_e$  or  $\nu_e$ , see for example H. Murayama and T. Yanagida, *Phys. Lett. B* **520**, 263 (2001). The Kam-2 Collaboration prefers to interpret all their 12 events as  $\bar{\nu}_e$  interactions; see [21] for a discussion.

- [7] LSND Collaboration, A. Aguilar *et al.*, *Phys. Rev. D* **64**, 112007 (2001).
- [8] MiniBooNE Collaboration, A. Bazarko, *Nucl. Phys. B (Proc. Suppl.)* **91**, 210 (2000).

- [9] B. Kayser, hep-ph/0104147.
- [10] D.O. Caldwell, G.M. Fuller, and Y.Z. Qian, Phys. Rev. D **61**, 123005 (2000).
- [11] Y.Z. Qian *et al.*, Phys. Rev. Lett. **71**, 1965 (1993).
- [12] F.J. Botella, C.S. Lim, and W.J. Marciano, Phys. Rev. D **35**, 896 (1987).
- [13] A.S. Dighe and A.Y. Smirnov, Phys. Rev. D **62**, 033007 (2000).
- [14] G. Barenboim *et al.*, hep-ph/0108199.
- [15] G. Barenboim, A.S. Dighe, and S. Skadhauge, Phys. Rev. D **65**, 053001 (2002).
- [16] V. Barger *et al.*, Phys. Rev. D **63**, 033002 (2001).
- [17] SNO Collaboration, Q.R. Ahmad *et al.*, Phys. Rev. Lett. **89**, 011301 (2002).
- [18] V. Barger *et al.*, Phys. Rev. D **58**, 093016 (1998).
- [19] Let us see what the effect of a possible violation of adiabaticity between the two highest energy eigenstates,  $\bar{\nu}_\mu$  and  $\bar{\nu}_\tau$  at high matter densities, in the case of a LSND-inverted (2+2) model [Fig. 1(f)] is on  $p_{e \rightarrow e}$  and  $p_{\mu \rightarrow e} + p_{\tau \rightarrow e}$ . Violation of adiabaticity would result in a non-vanishing hopping probability  $p_{hop}$  between these two local Hamiltonian eigenstates. Clearly,  $p_{e \rightarrow e}$  is unaffected, and also  $p_{\mu \rightarrow e} + p_{\tau \rightarrow e} = p_{hop}|U_{e0}^{evol}|^2 + (1 - p_{hop})|U_{e1}^{evol}|^2 + (1 - p_{hop})|U_{e0}^{evol}|^2 + p_{hop}|U_{e1}^{evol}|^2 = |U_{e0}^{evol}|^2 + |U_{e1}^{evol}|^2$  has the same value as in the adiabatic case.
- [20] C. Lunardini and A.Y. Smirnov, Nucl. Phys. **B616**, 307 (2001).
- [21] M. Koshiha, Phys. Rep. **220**, 229 (1992).
- [22] A.Y. Smirnov, D.N. Spergel, and J.N. Bahcall, Phys. Rev. D **49**, 1389 (1994).
- [23] KARMEN Collaboration, B. Armbruster *et al.*, Phys. Rev. D **65**, 112001 (2002); K. Eitel (private communication).
- [24] Y. Declais *et al.*, Nucl. Phys. **B434**, 503 (1995).
- [25] S.M. Bilenky *et al.*, Phys. Rev. D **54**, 1881 (1996); **60**, 073007 (1999).
- [26] O.L.G. Peres and A.Y. Smirnov, Nucl. Phys. **B599**, 3 (2001).
- [27] J.F. Beacom and P. Vogel, Phys. Rev. D **58**, 053010 (1998); **58**, 093012 (1998); L. Cadonati, F.P. Calaprice, and M.C. Chen, Astropart. Phys. **16**, 361 (2002); P. Vogel, Prog. Part. Nucl. Phys. **48**, 29 (2002); W. Fulgione, Nucl. Phys. B (Proc. Suppl.) **70**, 469 (1999); F. Halzen, J.E. Jacobsen, and E. Zas, Phys. Rev. D **53**, 7359 (1996); M. K. Sharp, J. F. Beacom, and J. A. Formaggio, *ibid.* **66**, 013012 (2002).
- [28] B. Jegerlehner, F. Neubig, and G. Raffelt, Phys. Rev. D **54**, 1194 (1996).

## 2.2 Short-baseline neutrino experiments and the number of neutrino species

As discussed in the previous Chapter, if the LSND observation of the  $\bar{\nu}_e$  excess in a  $\bar{\nu}_\mu$  neutrino beam is to be interpreted as  $\bar{\nu}_\mu \rightarrow \bar{\nu}_e$  oscillations, then additional, sterile neutrino species may be required to explain all of the experimental evidence on neutrino oscillations. Within these assumptions, short-baseline neutrino oscillation experiments provide constraints on the number of light sterile neutrino species, their masses and their mixings.

In the following paper (see Ref. [2] and references therein), written in collaboration with J. Conrad and M. Shaevitz, the constraints on sterile neutrino models from a combined analysis of several accelerator-based and reactor-based searches for  $\nu_\mu \rightarrow \nu_\mu$ ,  $\nu_e \rightarrow \nu_e$ , and  $\nu_\mu \rightarrow \nu_e$  oscillations at short baselines are presented. Neutrino models involving both one and two additional sterile neutrinos are studied. The first main result of this analysis is that (3+2) sterile neutrino models are significantly favored over (3+1) models. The second main result of the analysis is an estimate of the most likely and allowed values for the neutrino mass splittings and mixing matrix elements affecting the three oscillation channels listed above at short baselines, for both (3+1) and (3+2) models.

These results provide some guidance for present and future short-baseline oscillation searches, as well as for neutrino model building. In particular, this phenomenological work is of direct relevance to the MiniBooNE  $\nu_\mu$  disappearance analysis presented later in this thesis, and shows that sterile neutrino models may predict large (up to  $\sim 30\%$ )  $\nu_\mu$  disappearance in the  $\Delta m^2$  range probed by the MiniBooNE experiment.

# Combined analysis of short-baseline neutrino experiments in the $(3 + 1)$ and $(3 + 2)$ sterile neutrino oscillation hypotheses

M. Sorel,<sup>\*</sup> J. M. Conrad,<sup>†</sup> and M. H. Shaevitz<sup>‡</sup>

*Department of Physics, Columbia University, New York, New York 10027, USA*

(Received 21 April 2004; published 12 October 2004)

We investigate adding two sterile neutrinos to resolve the apparent tension existing between short-baseline neutrino oscillation results and CPT-conserving, four-neutrino oscillation models. For both  $(3 + 1)$  and  $(3 + 2)$  models, the level of statistical compatibility between the combined dataset from the null short-baseline experiments Bugey, CHOOZ, CCFR84, CDHS, KARMEN, and NOMAD, on the one hand; and the LSND dataset, on the other, is computed. A combined analysis of all seven short-baseline experiments, including LSND, is also performed, to obtain the favored regions in neutrino mass and mixing parameter space for both models. Finally, four statistical tests to compare the  $(3 + 1)$  and the  $(3 + 2)$  hypotheses are discussed. All tests show that  $(3 + 2)$  models fit the existing short-baseline data significantly better than  $(3 + 1)$  models.

DOI: 10.1103/PhysRevD.70.073004

PACS numbers: 14.60.Pq, 12.15.Ff, 14.60.St

## I. INTRODUCTION

There currently exist three experimental signatures for neutrino oscillations. The two signatures seen originally in solar and atmospheric neutrinos have been verified by several experiments, including experiments carried out with accelerator and nuclear reactor sources. The results on atmospheric neutrinos can be explained by  $\nu_\mu$  disappearance due to oscillations [1–3], while those on solar neutrinos can be explained by  $\nu_e$  oscillations [4,5]. The third signature is  $\bar{\nu}_e$  appearance in a  $\bar{\nu}_\mu$  beam, observed by the short-baseline, accelerator-based LSND experiment at Los Alamos [6]. This signature is strong from a statistical point of view, being a  $3.8\sigma$  excess, but further confirmation by an independent experiment is necessary. The MiniBooNE experiment at Fermilab will be able to confirm or refute the LSND signature in the near future, with an experimental setup providing different systematics and higher statistics than LSND [7].

Taken at face value, the three experimental signatures point to three independent mass splittings. Three neutrino masses do not appear to be able to explain all of the three signatures [8,9] (see, however, [10]). One way to solve this puzzle is to introduce different mass spectra for the neutrino and antineutrino sector, thereby requiring CPT violation but no extra neutrino generations [11]. Another possibility is to add additional neutrinos with no standard weak couplings, often called “sterile neutrinos.”

In this paper we assume CPT and CP invariance, and we explore the possibility of adding one- or two-neutrino generations beyond the three active flavors assumed by the Standard Model. We focus on extensions of the neutrino sector where the addition of fourth and fifth mass

eigenstates are responsible for the high  $\Delta m^2$  LSND oscillations, and the three lower mass states explain solar and atmospheric oscillations. When only one sterile neutrino is added, these models are labeled as  $(3 + 1)$ . The flavor content of the four-neutrino mass eigenstates for these models is schematically shown in Fig. 1(a). The  $(3 + 1)$  hierarchy in Fig. 1(a) is as opposed to the  $(2 + 2)$  hierarchy, where the solar and atmospheric mass splittings are separated from each other by the LSND  $\Delta m^2$ . The  $(2 + 2)$  models require a different global analysis from the one discussed in this paper. The simplest  $(2 + 2)$  models appear to be only marginally consistent with neutrino oscillations data [8,12], even though more general  $(2 + 2)$  mass and mixing scenarios might represent a viable solution to explain solar, atmospheric, and LSND oscillations [13].

The  $(3 + 1)$  models are motivated by the criterion of simplicity in physics, introducing the most minimal extension to the Standard Model that explains the experimental evidence. However, theories invoking sterile neutrinos to explain the origin of neutrino masses do not necessarily require only one sterile neutrino. Indeed, many popular realizations of the see-saw mechanism introduce three right-handed neutrino fields [14–16]. In particular,  $(3 + 2)$  neutrino mass and mixing models can be obtained in several see-saw mechanisms [17]. From the phenomenological point of view, it is our opinion that two- and three-sterile neutrino models should also be considered and confronted with existing experimental results. In this paper, we consider the results from the short-baseline experiments Bugey [18], CCFR84 [19], CDHS [20], CHOOZ [21], KARMEN [22], LSND [6], and NOMAD [23], and examine how well  $(3 + 1)$  and  $(3 + 2)$  models agree with data. A schematic diagram for  $(3 + 2)$  models is shown in Fig. 1(b). We do not consider  $(3 + 3)$  models in this paper. From our initial studies, we believe that the phenomenology of a  $(3 + 3)$  model is similar to a  $(3 + 2)$  model.

<sup>\*</sup>Electronic address: sorel@nevis.columbia.edu

<sup>†</sup>Electronic address: conrad@nevis.columbia.edu

<sup>‡</sup>Electronic address: shaevitz@nevis.columbia.edu

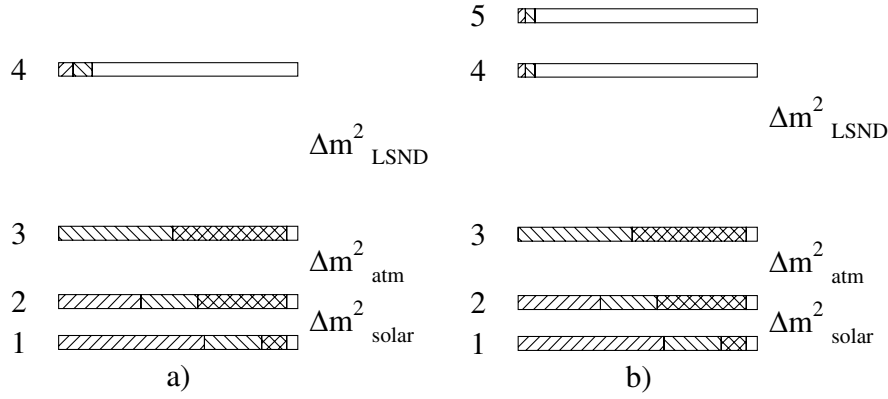


FIG. 1. Flavor content of neutrino mass eigenstates in (3 + 1) models (a), and (3 + 2) models (b). Neutrino masses increase from bottom to top. The  $\nu_e$  fractions are indicated by right-leaning hatches, the  $\nu_\mu$  fractions by left-leaning hatches, the  $\nu_\tau$  fractions by crosshatches, and the  $\nu_s$  fractions by no hatches. The flavor contents shown are schematic only.

The paper is organized as follows. In Sec. II, we specify the neutrino oscillations formalism used in this analysis to describe (3 + 1) and (3 + 2) short-baseline oscillations. In Sec. III and IV, we present the results obtained for the (3 + 1) and (3 + 2) models, respectively. For both models, we first derive the level of compatibility between the null short-baseline (NSBL) experiments and LSND. Second, we perform a combined analysis of all seven short-baseline experiments (including LSND) to derive the preferred regions in neutrino mass and mixing parameter space. In Sec. V, we discuss four statistical tests to compare the (3 + 1) and (3 + 2) hypotheses. In Sec. VI, we briefly mention other experimental constraints on (3 + 1) and (3 + 2) models. In the Appendix, we describe the physics and statistical assumptions used in the analysis to describe the short-baseline experiments.

## II. NEUTRINO OSCILLATIONS FORMALISM

Under the assumptions of CP and CPT invariance, the probability for a neutrino, produced with flavor  $\alpha$  and energy  $E$ , to be detected as a neutrino of flavor  $\beta$  after travelling a distance  $L$ , is [24]

$$P(\nu_\alpha \rightarrow \nu_\beta) = \delta_{\alpha\beta} - 4 \sum_{j>i}^n U_{\alpha,j} U_{\beta,j} U_{\alpha,i} U_{\beta,i} \sin^2 x_{ji}, \quad (1)$$

where  $\alpha = e, \mu, \tau, s$  ( $s$  being the sterile flavor);  $U$  is the unitary neutrino mixing matrix;  $x_{ji} \equiv 1.27 \Delta m_{ji}^2 L/E$ ;  $\Delta m_{ji}^2 \equiv m_j^2 - m_i^2$ ; and  $n$  is the number of neutrino generations. Neglecting CP-violating phases, there are in general  $(n - 1)$  independent mass splittings, and  $n^2 - n - n(n - 1)/2$  independent mixing matrix elements. The situation simplifies considerably by considering short-baseline (SBL) data only. In this case, it is a good approximation to assume  $x_{21} = x_{32} = 0$ , and only  $(n - 3)$  independent mass splittings are present. Moreover, given the set of SBL experiments considered, the number of

mixing matrix elements probed is only  $2(n - 3)$ , as we show now for the (3 + 1) and (3 + 2) cases.

For (3 + 1) models,  $n = 4$ , and only one mass splitting  $\Delta m^2 \equiv \Delta m_{41}^2 \simeq \Delta m_{42}^2 \simeq \Delta m_{43}^2$  appears in the oscillation formula: this is sometimes referred to as the “quasi two neutrino approximation,” or “one mass scale dominance” [25]. Using the unitarity properties of the mixing matrix, we can rewrite Eq. (1) for (3 + 1) models in a more convenient way

$$P(\nu_\alpha \rightarrow \nu_\beta) = \delta_{\alpha\beta} - 4U_{\alpha 4}U_{\beta 4}(\delta_{\alpha\beta} - U_{\alpha 4}U_{\beta 4})\sin^2 x_{41}, \quad (2)$$

which depends on the mass splitting ( $\Delta m_{41}^2$ ) and mixing parameters ( $U_{\alpha 4}, U_{\beta 4}$ ) of the fourth generation only. Since the two neutrino approximation is satisfied in the (3 + 1) case, we can express Eq. (2) in the usual forms

$$P(\nu_\alpha \rightarrow \nu_\beta) = \sin^2 2\theta_{\alpha\beta} \sin^2 x_{41}, \quad \alpha \neq \beta, \quad (3)$$

$$P(\nu_\alpha \rightarrow \nu_\alpha) = 1 - \sin^2 2\theta_{\alpha\alpha} \sin^2 x_{41}, \quad (4)$$

where Eq. (3) applies to an oscillation appearance measurement, Eq. (4) to a disappearance measurement.

In this paper, we use the data from the Bugey, CCFR84, CDHS, CHOOZ, KARMEN, LSND, and NOMAD experiments. Bugey and CHOOZ data constrain  $\nu_e$  disappearance; CCFR84 and CDHS data constrain  $\nu_\mu$  disappearance; and KARMEN, LSND, and NOMAD data constrain  $\nu_\mu \rightarrow \nu_e$  oscillations. Therefore, from Eqs. (2)–(4), the experiments constrain the following combinations of (3 + 1) mixing parameters:

- (i) Bugey, CHOOZ:  $\sin^2 2\theta_{ee} \equiv 4U_{e4}^2(1 - U_{e4}^2)$ ;
- (ii) CCFR84, CDHS:  $\sin^2 2\theta_{\mu\mu} \equiv 4U_{\mu 4}^2(1 - U_{\mu 4}^2)$ ;
- (iii) KARMEN, LSND, NOMAD:  $\sin^2 2\theta_{\mu e} \equiv 4U_{e4}^2 U_{\mu 4}^2$ .

In (3 + 1) models, the tension between the experimental results comes about because Bugey, CHOOZ, CCFR84, CDHS, KARMEN, and NOMAD limit the two

independent mixing matrix parameters  $U_{e4}$  and  $U_{\mu4}$  to be small, whereas LSND demands nonzero values.

In (3 + 2) models, we introduce two sterile neutrinos. Using Eq. (1) and the unitarity of the mixing matrix, the (3 + 2) neutrino oscillation probability formula can be written

$$P(\nu_\alpha \rightarrow \nu_\beta) = \delta_{\alpha\beta} - 4[(\delta_{\alpha\beta} - U_{\alpha4}U_{\beta4} - U_{\alpha5}U_{\beta5})(U_{\alpha4}U_{\beta4}\sin^2 x_{41} + U_{\alpha5}U_{\beta5}\sin^2 x_{51}) + U_{\alpha4}U_{\alpha5}U_{\beta4}U_{\beta5}\sin^2 x_{54}] = \delta_{\alpha\beta} + 4[U_{\alpha4}^2(U_{\beta4}^2 - \delta_{\alpha\beta})\sin^2 x_{41} + U_{\alpha5}^2(U_{\beta5}^2 - \delta_{\alpha\beta})\sin^2 x_{51} + U_{\alpha4}U_{\beta4}U_{\alpha5}U_{\beta5}(\sin^2 x_{41} + \sin^2 x_{51} - \sin^2 x_{54})], \quad (5)$$

which in our case depends on two independent mass splittings ( $\Delta m_{41}^2, \Delta m_{51}^2$ ) and four independent mixing matrix parameters ( $U_{\alpha4}, U_{\alpha5}$ , with  $\alpha = e, \mu$ ). Equation (2) can be recovered from Eq. (5) by requiring  $U_{\alpha5} = U_{\beta5} = 0$ . In (3 + 2) models, the quasi two neutrino approximation is not valid, since there are three distinct  $\Delta m^2$  values contributing in the oscillation formula:  $\Delta m_{41}^2$ ,  $\Delta m_{51}^2$ , and  $\Delta m_{54}^2$ , and therefore three distinct oscillation amplitudes:  $(\sin^2 2\theta_{\alpha\beta})_{41}$ ,  $(\sin^2 2\theta_{\alpha\beta})_{51}$ , and  $(\sin^2 2\theta_{\alpha\beta})_{54}$ .

We now comment on the Monte Carlo method used to apply the above oscillation formalism to the analyses presented in this paper. We require the neutrino mass splittings to be in the range  $0.1 \text{ eV}^2 \leq \Delta m_{41}^2, \Delta m_{51}^2 \leq 100 \text{ eV}^2$ , with  $\Delta m_{51}^2 \geq \Delta m_{41}^2$ . Each mass splitting range is analyzed over a 200 point grid, uniformly in  $\log_{10} \Delta m^2$ . In Sec. VI, we briefly discuss why large mass splittings are not necessarily in contradiction with cosmological (and other) data. The values of the mixing parameters,  $U_{e4}$ ,  $U_{\mu4}$ ,  $U_{e5}$ , and  $U_{\mu5}$ , are randomly generated over a four-dimensional space satisfying the four requirements:  $U_{ei}^2 + U_{\mu i}^2 \leq 0.5$ ,  $U_{\alpha4}^2 + U_{\alpha5}^2 \leq 0.5$ , where  $i = 4, 5$ ,  $\alpha = e, \mu$ . These four inequalities are introduced to account for the fact that large electron and muon flavor fractions in the fourth and fifth mass eigenstates are not allowed by solar and atmospheric neutrino data. In principle, since the CDHS constraint on  $\nu_\mu$  disappearance vanishes for  $\Delta m^2 \simeq 0.3 \text{ eV}^2$ , as shown in the Appendix, the upper limit on  $\nu_\mu$  disappearance from atmospheric neutrino experiments above the atmospheric  $\Delta m^2$  should be considered instead. In this paper, we do not reconstruct the likelihood for atmospheric data that would give the exclusion region for  $\nu_\mu$  disappearance in the range  $\Delta m_{atm}^2 \ll \Delta m^2 < 0.3 \text{ eV}^2$ . However, the effect that the atmospheric constraints would have on our results is expected to be small. For example, in Ref. [26], Bilenky *et al.* use the atmospheric up-down asymmetry to derive the upper limit  $U_{\mu4}^2 < 0.55$  at 90% CL for (3 + 1) models, which is satisfied by our initial requirements  $U_{e4}^2 + U_{\mu4}^2 < 0.5$ ,  $U_{\mu4}^2 + U_{\mu5}^2 < 0.5$ . A more recent analysis [27] of atmospheric neutrino data using the full zenith angle distribution provides a tighter constraint on  $\sin^2 \theta_{\mu\mu}$  than the one given in Ref. [26]; the impact of this additional constraint on our SBL analysis is discussed in Sections III and VI. Finally, from Eqs. (2), it is clear that the relative sign of both  $U_{e4}$  and  $U_{\mu4}$  cannot be inferred

in (3 + 1) oscillations. Similarly, from Eq. (5), the only physically observable relative sign between mixing parameters in CP-conserving (3 + 2) models is  $\text{sign}(U_{e4}U_{\mu4}U_{e5}U_{\mu5})$ ; therefore, this is the only sign related to mixing parameters that we randomly generate in the analysis.

Throughout the paper, we make use of the Gaussian approximation in determining allowed regions in parameter space. In general, this means that the regions of quoted confidence level are the ones enclosed by contours of constant  $\chi^2$  values, whose differences with respect to the best-fit  $\chi^2$  value depend on the number of free parameters in the model [28]. In the text, we use the symbol  $\delta$  to denote the values of the confidence levels derived in this way. As pointed out in [29], this approach should be considered approximate, as it may provide regions in parameter space of both higher and lower confidence than the one quoted. Regions of higher confidence than the quoted value may result from the presence of highly correlated parameters. Regions of lower confidence may result from the presence of fast oscillatory behavior of the oscillation probability formula, Eq. (1).

### III. RESULTS FOR (3 + 1) MODELS

This section, like the next one on (3 + 2) models, consists of two parts. First, we quantify the statistical compatibility between the NSBL and LSND results, following a method described in [30,31], originally proposed to establish the compatibility between the LSND and KARMEN results. Second, we perform a combined analysis of the NSBL and LSND datasets, to obtain the favored regions in neutrino mass and mixing parameter space.

#### A. Statistical compatibility between NSBL and LSND

Many analyses of the NSBL experiments within (3 + 1) models have concluded that the allowed LSND region is largely excluded [32–34]. Here, we repeat this study with two purposes. First, we use this study to give context to our discussion of the basic model and techniques which will be expanded in later sections. Second, we demonstrate that our fit, which forms the basis of our new results for (3 + 2) models, reproduces the expected (3 + 1) exclusion region. For a discussion of the physics and statistical assumptions used to describe the short-baseline



experiments used in the analysis, the reader should refer to the Appendix.

In this section, the NSBL and LSND datasets are analyzed separately, providing two independent allowed regions in  $(\sin^2 2\theta_{\mu e}, \Delta m^2)$  space. The level of statistical compatibility between the two datasets can be determined by studying to what degree the two allowed regions overlap, as will be quantified later in this section.

For each randomly generated  $(3 + 1)$  model, we calculate the values for the  $\chi^2$  functions  $\chi^2_{\text{NSBL}}$  and  $\chi^2_{\text{LSND}}$ , where  $\chi^2_{\text{NSBL}}$  is defined as

$$\chi^2_{\text{NSBL}} \equiv \chi^2_{\text{Bugey}} + \chi^2_{\text{CHOOZ}} + \chi^2_{\text{CCFR84}} + \chi^2_{\text{CDHS}} + \chi^2_{\text{KARMEN}} + \chi^2_{\text{NOMAD}}. \quad (6)$$

For the analysis described in this section, the NSBL and LSND allowed regions are obtained using two different algorithms, reflecting the fact that the NSBL dataset provides upper limits on oscillations, while the LSND dataset points to non-null oscillations.

The NSBL allowed regions at various confidence levels  $\delta_{\text{NSBL}}$  are obtained via a raster scan algorithm [29]. Let  $\chi^2_{\text{NSBL}}$  be the  $\chi^2$  value for the particular model and  $(\chi^2_{\text{NSBL}})_{\min, \Delta m^2}$  be the minimum  $\chi^2$  for the  $\Delta m^2$  value considered. For example, our quoted 95% CL upper limit on  $\sin^2 2\theta_{\mu e}$  is given by the maximum value for the product  $4U_{e4}^2 U_{\mu 4}^2$  chosen among the models which satisfy the inequality  $\chi^2_{\text{NSBL}} - (\chi^2_{\text{NSBL}})_{\min, \Delta m^2} < 5.99$ . The value of 5.99 units of  $\chi^2$  is chosen because there are two free

parameters  $U_{e4}, U_{\mu 4}$  for  $(3 + 1)$  models with fixed  $\Delta m^2$ . We note that even for the NSBL dataset, the parameters  $U_{e4}, U_{\mu 4}$  can be correlated, since the KARMEN and NOMAD results probe a combination of the two parameters.

The LSND allowed regions at various confidence levels  $\delta_{\text{LSND}}$  are obtained via a global scan algorithm [29]. For example, for  $\delta_{\text{LSND}} = 0.95$  we require  $\chi^2_{\text{LSND}} - (\chi^2_{\text{LSND}})_{\min} < 5.99$ , where  $(\chi^2_{\text{LSND}})_{\min}$  is now the global LSND  $\chi^2$  minimum value, considering all possible  $\Delta m^2$  values. The LSND allowed region is computed for two free parameters as for the NSBL case, but the parameters are now  $\Delta m^2$  and  $U_{\mu 4} U_{e4}$ , as opposed to  $U_{\mu 4}$  and  $U_{e4}$ . Compared to the NSBL case, the number of free parameters is reduced by one because the LSND  $\bar{\nu}_\mu \rightarrow \bar{\nu}_e$  search only probes the product  $U_{\mu 4} U_{e4}$  and not the two mixing matrix elements individually, and it is increased by one because the allowed region is now obtained by scanning over all possible  $\Delta m^2$  values.

The regions allowed in  $(\sin^2 2\theta_{\mu e}, \Delta m^2)$  parameter space by both the NSBL and LSND datasets are shown in Fig. 2(a). The NSBL allowed regions shown are two-dimensional projections of three-dimensional allowed regions in  $(\Delta m^2, U_{e4}, U_{\mu 4})$  space. The NSBL results alone allow the regions to the left of the solid gray, dotted black, and solid black lines in the Fig. 2(a), at a confidence level  $\delta_{\text{NSBL}} = 0.90, 0.95, 0.99$ , respectively. In Fig. 2(a), the  $\delta_{\text{LSND}} = 0.90, 0.95, 0.99$  CL allowed regions obtained by our analysis for LSND data are also

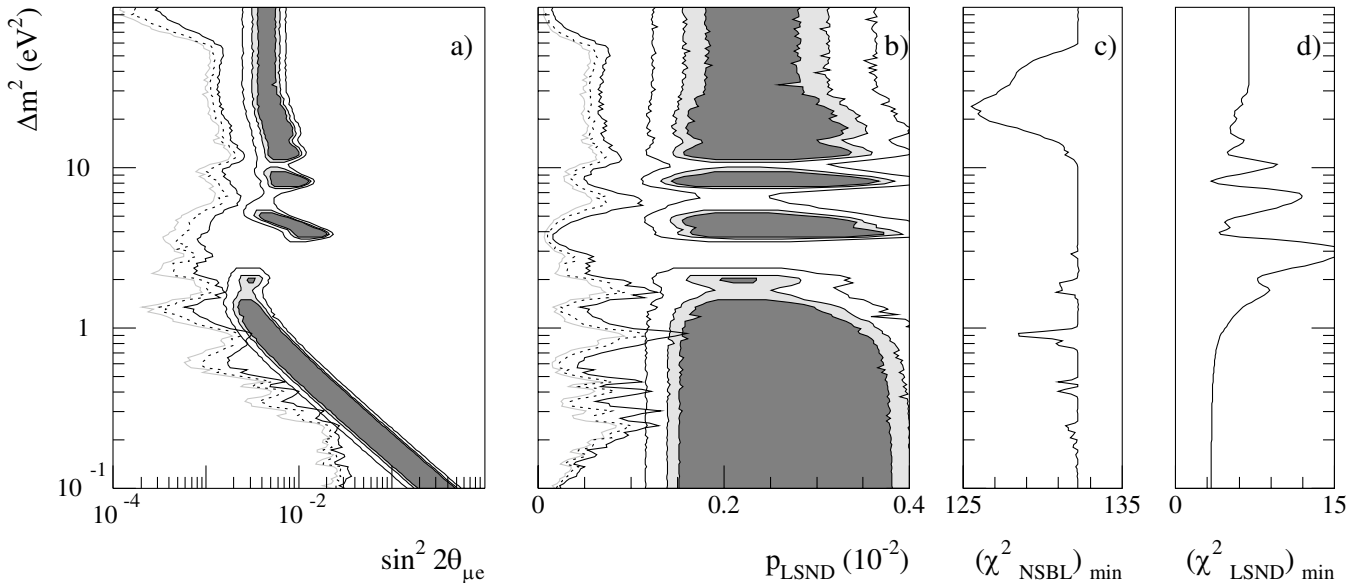


FIG. 2. Compatibility between the NSBL and LSND datasets in  $(3 + 1)$  models. Figure (a) shows the 90% (gray solid line), 95% (black dotted line), and 99% (black solid line) CL exclusion curves in  $(\sin^2 2\theta_{\mu e}, \Delta m^2)$  space for  $(3 + 1)$  models, considering the null short-baseline (NSBL) experiments Bugey, CCFR84, CDHS, CHOOZ, KARMEN, and NOMAD. Figure (b) also shows the 90%, 95%, and 99% CL allowed regions by our analysis of LSND data. Figure (b) is as Figure (a), but in  $(p_{\text{LSND}}, \Delta m^2)$  space, where  $p_{\text{LSND}}$  is the LSND oscillation probability (see text for the definition). Figures (c) and (d) show the minimum  $\chi^2$  values as a function of  $\Delta m^2$  for the NSBL and LSND datasets (143 and three d.o.f., respectively).

shown, as dark gray shaded, light gray shaded, and white areas, respectively. We find no overlap between the two individual 95% CL allowed regions; on the other hand, there is overlap between the two 99% CL regions.

Figure 2(b) shows the same  $(3 + 1)$  allowed regions as Fig. 2(a) but in the  $(p_{\text{LSND}}, \Delta m^2)$  plane, where  $p_{\text{LSND}}$  is defined as the  $\nu_\mu \rightarrow \nu_e$  oscillation probability averaged over the LSND  $L/E$  distribution

$$p_{\text{LSND}} \equiv \langle P(\nu_\mu \rightarrow \nu_e) \rangle, \quad (7)$$

where  $P(\nu_\mu \rightarrow \nu_e)$  is given by Eq. (1) for  $\alpha = \mu$ ,  $\beta = e$ , and is a function of all the mass and mixing parameters of the oscillation model under consideration. This has the obvious disadvantage of being a quantity dependent upon the specifics of a certain experiment, as opposed to a universal variable such as  $\sin^2 2\theta_{\mu e} = 4U_{\mu 4}^2 U_{e 4}^2$ . However,  $p_{\text{LSND}}$  has the advantage of being unambiguously defined for any number of neutrino generations, and thus is useful in discussing  $(3 + 2)$  models later in this paper. As stated previously, the oscillation probability estimator  $\sin^2 2\theta_{\mu e} = 4U_{\mu 4}^2 U_{e 4}^2$  cannot be used when more than one  $\Delta m^2$  value affects the oscillation probability, as is the case for  $(3 + 2)$  models. A second advantage of using  $p_{\text{LSND}}$  instead of  $\sin^2 2\theta_{\mu e}$  as the oscillation probability estimator, is that the allowed values for  $p_{\text{LSND}}$  inferred from the LSND result tend to be almost  $\Delta m^2$ -independent (see gray-shaded areas in Fig. 2(b)), as expected for an almost pure counting experiment such as LSND. The oscillation probability reported by the LSND collaboration [6] is  $p_{\text{LSND}} = (0.264 \pm 0.067 \pm 0.045)\%$ , and agrees well with our result of Fig. 2(b).

Figure 2(c) shows the values for  $(\chi_{\text{NSBL}}^2)_{\min}$  as a function of  $\Delta m^2$ . The number of degrees of freedom is 143. As discussed in the Appendix, the dip in  $(\chi_{\text{NSBL}}^2)_{\min}$  at  $\Delta m^2 \simeq 0.9 \text{ eV}^2$  is due to Bugey data preferring  $U_{e 4} \neq 0$  values,

while the minimum at  $\Delta m^2 \sim 10 - 30 \text{ eV}^2$  is due to CDHS (mostly) and CCFR84 data, preferring  $U_{\mu 4} \neq 0$  values. The  $\chi^2$  value for no-oscillations,  $(\chi_{\text{NSBL}}^2)_{\text{noosc}} = 132.2$ , is the largest  $\chi^2$  value in Fig. 2(c); this means that the choice of parameters  $U_{e 4} = U_{\mu 4} = 0$  provides the best-fit to NSBL data, for the  $\Delta m^2$  values satisfying the condition  $(\chi_{\text{NSBL}}^2)_{\min} = (\chi_{\text{NSBL}}^2)_{\text{noosc}}$ . Note that the  $\Delta m^2 \simeq 0.9 \text{ eV}^2$ ,  $\Delta m^2 \simeq 10 - 30 \text{ eV}^2$  dips in  $\chi_{\text{NSBL}}^2$  are consistent with  $U_{e 4} U_{\mu 4} = 0$ , and therefore with  $\sin^2 2\theta_{\mu e} = p_{\text{LSND}} = 0$ , but give better fits than the no-oscillations hypothesis,  $U_{e 4} = U_{\mu 4} = 0$ . In other words, the goodness of fit for the  $\sin^2 2\theta_{\mu e} = p_{\text{LSND}} = 0$  region depends on the  $\Delta m^2$  value considered.

Similarly, Fig. 2(d) shows the values for  $(\chi_{\text{LSND}}^2)_{\min}$  as a function of  $\Delta m^2$ , used to obtain the LSND allowed regions drawn in Figs. 2(a) and 2(b).

We now present a slightly different approach to determine the statistical compatibility between the NSBL and LSND datasets in  $(3 + 1)$  models, which will prove useful in comparing the  $(3 + 1)$  and  $(3 + 2)$  hypotheses.

In Fig. 3, we show the values for the  $\chi^2$  differences  $\Delta\chi_{\text{NSBL}}^2$ ,  $\Delta\chi_{\text{LSND}}^2$ , as well as the corresponding confidence levels  $\delta_{\text{NSBL}}$ ,  $\delta_{\text{LSND}}$ , as a function of the LSND oscillation probability. The curves are for the set of  $(3 + 1)$  models with the neutrino mass splitting  $\Delta m^2$  fixed to the best-fit value obtained in a combined NSBL + LSND analysis (see Sec. III B),  $\Delta m^2 = 0.92 \text{ eV}^2$ , and mixing matrix elements  $U_{\mu 4}$ ,  $U_{e 4}$  treated as free parameters. The value for  $\Delta m^2$  is chosen in this way because it represents to a good approximation the value for which one expects the best compatibility between the two datasets, as can also be seen in Fig. 2(b). In Fig. 3(a), we map the  $(U_{e 4}, U_{\mu 4})$  allowed space into the  $(p_{\text{LSND}}, \chi_{\text{NSBL}}^2)$ ,  $(p_{\text{LSND}}, \chi_{\text{LSND}}^2)$  spaces. For any given value of  $p_{\text{LSND}}$ , the minima for the  $\chi_{\text{NSBL}}^2$  and  $\chi_{\text{LSND}}^2$  functions are found

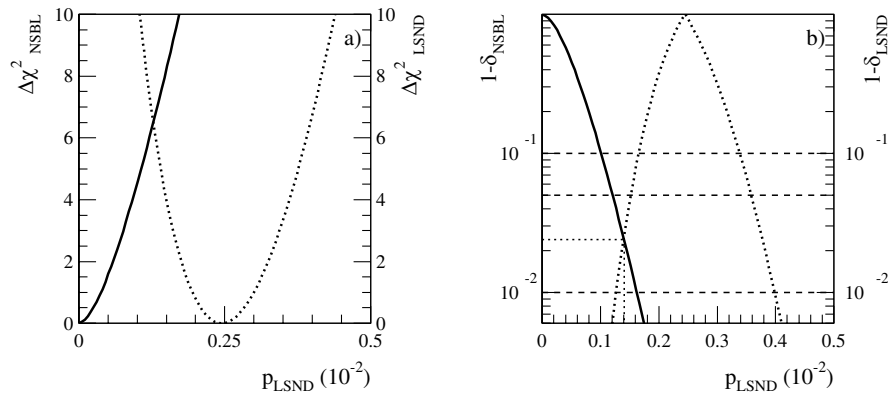


FIG. 3. (a)  $\chi^2$  differences  $\Delta\chi_{\text{NSBL}}^2$ ,  $\Delta\chi_{\text{LSND}}^2$ , and (b) individual confidence levels  $\delta_{\text{NSBL}}$ ,  $\delta_{\text{LSND}}$ , as a function of the LSND oscillation probability  $p_{\text{LSND}}$ , for the NSBL and LSND datasets. The curves are for  $(3 + 1)$  models with the neutrino mass splitting  $\Delta m^2$  fixed to the best-fit value  $\Delta m^2 = 0.92 \text{ eV}^2$  from the combined NSBL + LSND analysis, and variable mixing matrix elements  $U_{\mu 4}$ ,  $U_{e 4}$ . The solid curves refer to the NSBL dataset, the dotted ones to the LSND dataset. The dashed horizontal lines in Figure (b) refer to the 90%, 95%, 99% individual confidence levels, the dotted horizontal line gives the combined confidence level  $\delta = \delta_{\text{NSBL}}[\delta_{\text{LSND}} + (1 - \delta_{\text{LSND}})/2]$  for which the NSBL and LSND datasets are incompatible.

in the two  $(U_{e4}, U_{\mu4})$  and one  $(U_{e4}U_{\mu4})$  free parameters available, respectively. The process is repeated for several  $p_{\text{LSND}}$  values, and the collection of these minima for all values of  $p_{\text{LSND}}$  give the two curves in Fig. 3(a). The individual confidence levels  $\delta_{\text{NSBL}}$ ,  $\delta_{\text{LSND}}$ , shown in Fig. 3(b), are obtained from  $\Delta\chi^2_{\text{NSBL}}$ ,  $\Delta\chi^2_{\text{LSND}}$  in the usual way, by assuming one and two free parameters for the LSND and NSBL datasets, respectively.

We now address how to extract areas in parameter space of a given combined confidence  $\delta$  from two independent experimental constraints, in our case obtained via the NSBL and LSND datasets, without assuming statistical compatibility *a priori*. The most straightforward way (described, for example, in [30,31]) is to assign a confidence level  $\delta = \delta_{\text{NSBL}}[\delta_{\text{LSND}} + (1 - \delta_{\text{LSND}})/2]$  to the overlapping part (if any) between the two separate allowed regions in parameter space which are found with the constraint  $\delta_{\text{NSBL}} = \delta_{\text{LSND}}$ . The extra factor  $(1 - \delta_{\text{LSND}})/2$  is due to the fact that the LSND allowed region in the oscillation probability is two-sided, and overlap with the NSBL result on the same probability is obtained only for downward fluctuations in the LSND result, and not for upward ones.

From Fig. 3(b), we find overlapping allowed ranges in  $p_{\text{LSND}}$  for  $1 - \delta_{\text{NSBL}} = 1 - \delta_{\text{LSND}} \simeq 2.4\%$ . We conclude that, in  $(3 + 1)$  models, the LSND and NSBL datasets are incompatible at a combined confidence of  $\delta \simeq 96.4\%$ . In our opinion, this value does not support any conclusive statements against the statistical compatibility between NSBL and LSND data in  $(3 + 1)$  models, although it

represents poor agreement between the two datasets. The reader should also refer to Sec. V D, where a different method to quantify the compatibility between the NSBL and LSND results is discussed. Future short-baseline constraints on  $\nu_\mu \rightarrow \nu_e$  appearance, as well as on  $\nu_\mu$  and  $\nu_e$  disappearance, should be able to definitively establish whether  $(3 + 1)$  models are a viable solution to explain the LSND signal.

### B. Combined NSBL + LSND analysis

The second analysis we perform is a combined NSBL + LSND analysis, with the purpose of obtaining the  $(3 + 1)$  allowed regions in parameter space, in both  $(\sin^2 2\theta_{\mu e}, \Delta m^2)$  and  $(p_{\text{LSND}}, \Delta m^2)$  space. A combined analysis of this sort assumes statistically compatible results. In Sec. III A, we have shown that the LSND and NSBL results are marginally compatible, for  $(3 + 1)$  models. In the following, we refer to the NSBL + LSND dataset as the short-baseline (SBL) dataset, and we construct the  $\chi^2$  function

$$\chi^2_{\text{SBL}} \equiv \chi^2_{\text{NSBL}} + \chi^2_{\text{LSND}}, \quad (8)$$

where the two contributions  $\chi^2_{\text{NSBL}}$  and  $\chi^2_{\text{LSND}}$  are now simultaneously minimized with respect to the same set of three oscillation parameters  $\Delta m^2$ ,  $U_{e4}$ ,  $U_{\mu4}$ .

Figures 4(a) and 4(b) show the 90%, 95%, and 99% CL three-dimensional allowed regions in  $(\Delta m^2, U_{e4}, U_{\mu4})$  projected onto the  $(\sin^2 2\theta_{\mu e}, \Delta m^2)$  and  $(p_{\text{LSND}}, \Delta m^2)$  two-dimensional regions, respectively, from the com-

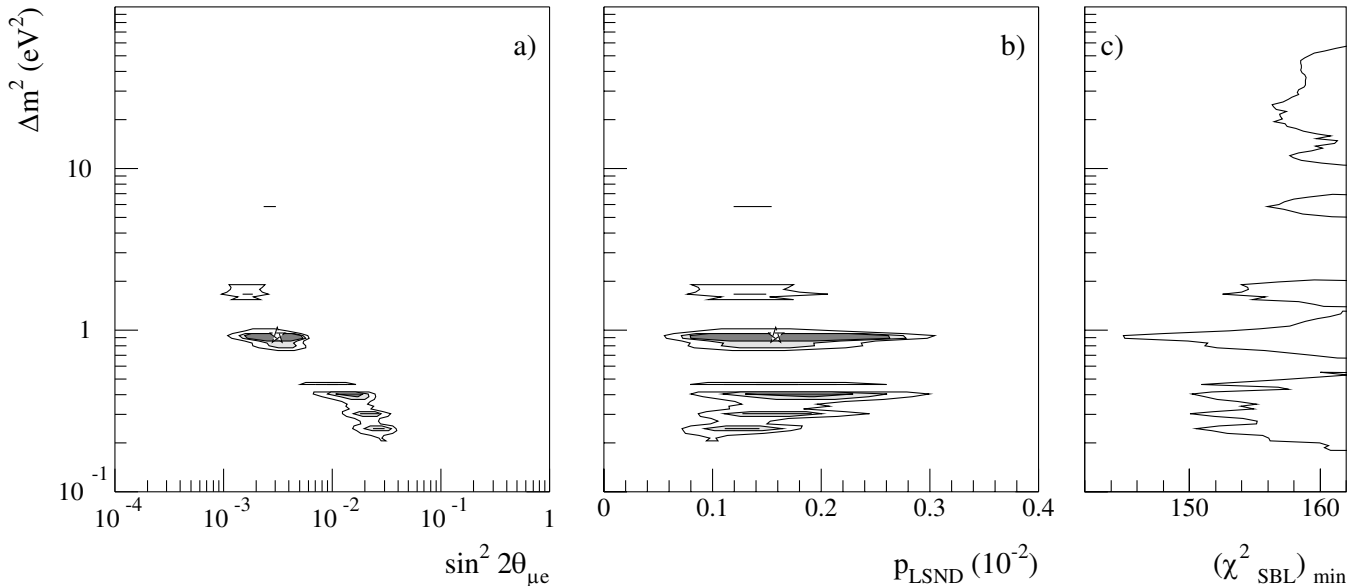


FIG. 4. Allowed regions in parameter space from a combined analysis of NSBL and LSND data, in  $(3 + 1)$  models, assuming statistical compatibility of the NSBL and LSND datasets. Figure (a) shows the 90%, 95%, and 99% CL allowed regions in  $(\sin^2 2\theta_{\mu e}, \Delta m^2)$  space, together with the best-fit point, indicated by the star; (b) shows the same allowed regions in  $(p_{\text{LSND}}, \Delta m^2)$  space; (c) shows the minimum  $\chi^2$  value obtained in the combined analysis as a function of  $\Delta m^2$ . The number of degrees of freedom is 148.

bined (3 + 1) analysis of SBL data. In this combined analysis, we use the same Monte Carlo method described in Sec. III A. We define the allowed regions in parameter space by performing a global scan. For example, the 95% CL allowed region in the three-dimensional space  $(\Delta m^2, U_{e4}, U_{\mu 4})$  is obtained by requiring  $\chi^2_{\text{SBL}} - (\chi^2_{\text{SBL}})_{\min} < 7.82$ , where  $(\chi^2_{\text{SBL}})_{\min}$  is the global minimum  $\chi^2$  value. Figure 4(c) shows the minimum  $\chi^2_{\text{SBL}}$  values obtained in the combined fit, as a function of  $\Delta m^2$ . Of course, the  $\chi^2_{\text{SBL}}$  values shown in Fig. 4(c) for any given  $\Delta m^2$  value are larger than the sum of the two contributions  $\chi^2_{\text{NSBL}}, \chi^2_{\text{LSND}}$ , shown in Figs. 2(c) and 2(d), for the same  $\Delta m^2$  value, since the latter were separately minimized with respect to the oscillation parameters. Similarly, Figs. 5(a) and 5(b) show the projections of the 90%, 95%, and 99% CL allowed regions in  $(\Delta m^2, U_{e4}, U_{\mu 4})$  onto the  $(\sin^2 2\theta_{ee}, \Delta m^2)$  and  $(\sin^2 2\theta_{\mu\mu}, \Delta m^2)$  space, respectively, from the combined (3 + 1) analysis of SBL data. The zenith angle distribution of atmospheric muon neutrinos provides a constraint to  $\sin^2 \theta_{\mu\mu}$  that is not included in this SBL analysis; mixings to the right of the dashed vertical line in Fig. 5(b) are excluded at 90% CL by atmospheric neutrino results [27]. The global  $\chi^2$  minimum is  $\chi^2_{\text{SBL}} = 144.9$  (148 d.o.f.). This  $\chi^2$  value indicates an acceptable fit, assuming that the goodness-of-fit statistic follows the standard  $\chi^2$  p.d.f. [25]; for an alternative goodness-of-fit test, the reader should refer to Sec. V D. The individual NSBL and LSND contributions to the  $\chi^2$  minimum are  $\chi^2_{\text{NSBL}} = 137.3$  and  $\chi^2_{\text{LSND}} = 7.6$ , respectively. This best-fit point corresponds to the mass and mixing parameters  $\Delta m^2 = 0.92 \text{ eV}^2$ ,  $U_{e4} = 0.136$ ,  $U_{\mu 4} = 0.205$ .

## IV. RESULTS FOR (3 + 2) MODELS

### A. Statistical compatibility between NSBL and LSND

Having introduced the relevant oscillation probability formula in Eq. (5), and the statistical estimator  $p_{\text{LSND}}$  to compare the NSBL and LSND results in Sec. III A, we can now quantitatively address the statistical compatibility between the NSBL and LSND datasets under the (3 + 2) hypothesis.

Ideally, we would like to determine the NSBL upper limit for  $p_{\text{LSND}}$ , for all possible combinations of the mass parameters  $\Delta m^2_{41}, \Delta m^2_{51}$ . This entails performing a scan equivalent to the one described in the (3 + 1) case as a function of  $\Delta m^2_{41}$ , shown in Fig. 2. In practice, the CPU-time requirements to pursue this route were prohibitive.

An easier problem to tackle is to determine the statistical compatibility between the NSBL and LSND datasets only for the (3 + 2) models with mass splittings  $\Delta m^2_{41}, \Delta m^2_{51}$  fixed to their best-fit values, as obtained by the combined NSBL + LSND analysis that we present in Sec. IV B. In Sections III A and III B, we have demonstrated that, at least for (3 + 1) models, this choice is a good approximation for the best possible statistical compatibility (see Figs. 2 and 4).

In Fig. 6, we show the behavior of the  $\chi^2$  values  $\Delta \chi^2_{\text{NSBL}}$  and  $\Delta \chi^2_{\text{LSND}}$ , and of the confidence levels  $\delta_{\text{NSBL}}$  and  $\delta_{\text{LSND}}$ , as a function of  $p_{\text{LSND}}$ , for the set of (3 + 2) models satisfying the requirements  $\Delta m^2_{41} = 0.92 \text{ eV}^2$ ,  $\Delta m^2_{51} = 22 \text{ eV}^2$ . By analogy with Fig. 3, we map the four-dimensional space  $(U_{e4}, U_{\mu 4}, U_{e5}, U_{\mu 5})$  into the two-dimensional spaces  $(p_{\text{LSND}}, \chi^2_{\text{NSBL}})$  and  $(p_{\text{LSND}}, \chi^2_{\text{SBL}})$ , and we plot the minimum  $\chi^2$  values

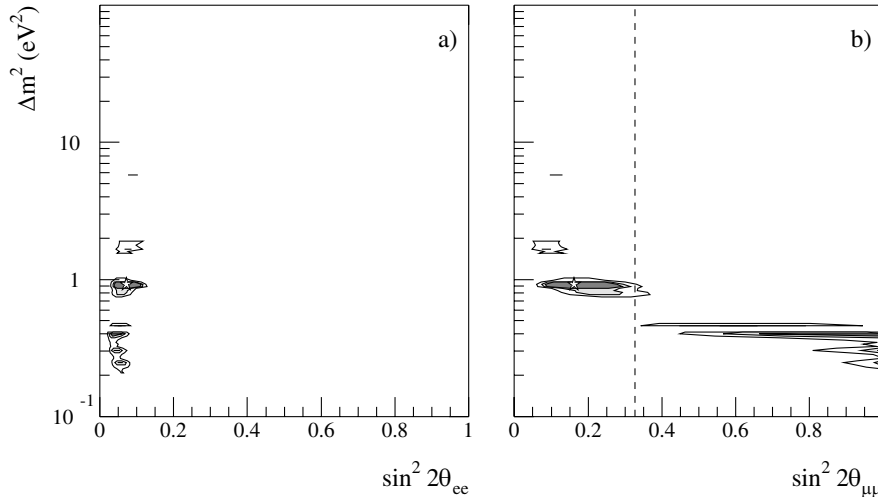


FIG. 5. Allowed regions in the parameter spaces relevant for  $\nu_e$  and  $\nu_\mu$  disappearance from a combined analysis of NSBL and LSND data, in (3 + 1) models, assuming statistical compatibility of the NSBL and LSND datasets. Figure (a) shows the 90%, 95%, and 99% CL allowed regions in  $(\sin^2 2\theta_{ee}, \Delta m^2)$  space, together with the best-fit point, indicated by the star; (b) shows the same allowed regions in  $(\sin^2 2\theta_{\mu\mu}, \Delta m^2)$  space. Mixings to the right of the dashed vertical line in Figure (b) are excluded at 90% CL by atmospheric neutrino results [27], which are not included in this analysis.

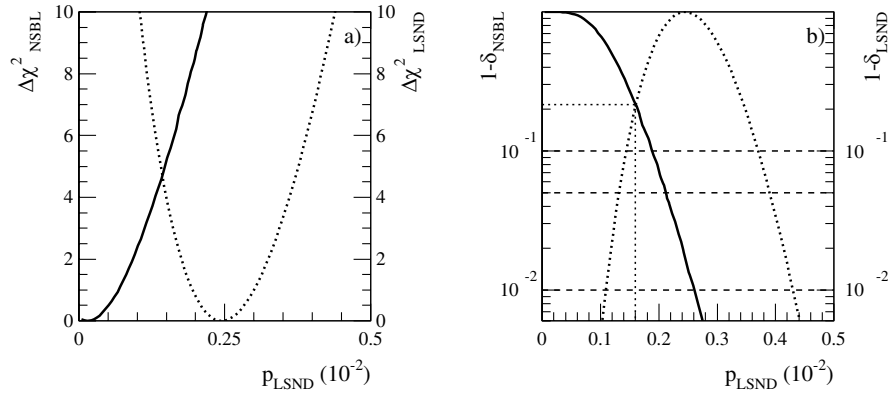


FIG. 6. (a)  $\chi^2$  differences  $\Delta\chi^2_{\text{NSBL}}$  and  $\Delta\chi^2_{\text{LSND}}$ , and (b) individual confidence levels  $\delta_{\text{NSBL}}$  and  $\delta_{\text{LSND}}$ , as a function of the LSND oscillation probability  $p_{\text{LSND}}$ , for the NSBL and LSND datasets. The curves are for  $(3 + 2)$  models with the neutrino mass splittings  $\Delta m^2_{41}$  and  $\Delta m^2_{51}$ , fixed to the best-fit values  $\Delta m^2_{41} = 0.92 \text{ eV}^2$ ,  $\Delta m^2_{51} = 22 \text{ eV}^2$  from the combined NSBL + LSND analysis, and variable mixing matrix elements  $U_{e4}$ ,  $U_{\mu 4}$ ,  $U_{e5}$ ,  $U_{\mu 5}$ . The solid curves refer to the NSBL dataset, the dotted ones to the LSND dataset. The dashed horizontal lines in Figure (b) refer to the 90%, 95%, 99% individual confidence levels; the dotted horizontal line gives the combined confidence level  $\delta = \delta_{\text{NSBL}}[\delta_{\text{LSND}} + (1 - \delta_{\text{LSND}})/2]$  for which the NSBL and LSND datasets are incompatible.

obtained for any given value of  $p_{\text{LSND}}$ . The confidence levels shown in Fig. 6(b) are obtained from Fig. 6(a) considering the four free parameters ( $U_{e4}$ ,  $U_{\mu 4}$ ,  $U_{e5}$ ,  $U_{\mu 5}$ ) in the  $\chi^2_{\text{NSBL}}$  minimization process, and the two free parameters ( $U_{e4}U_{\mu 4}$ ,  $U_{e5}U_{\mu 5}$ ) for  $\chi^2_{\text{LSND}}$ .

From Fig. 6(b), we find that, in  $(3 + 2)$  models, the NSBL and LSND datasets are incompatible at an individual confidence level of  $\delta_{\text{NSBL}} = \delta_{\text{LSND}} = 1 - 0.215 = 78.5\%$ , and at a combined confidence level  $\delta = \delta_{\text{NSBL}}[\delta_{\text{LSND}} + (1 - \delta_{\text{LSND}})/2] = 70.0\%$ . Figure 6 should be compared to Fig. 3, obtained for  $(3 + 1)$  models. A detailed comparison of the  $(3 + 1)$  and  $(3 + 2)$  hypotheses is presented in Sec. V.

### B. Combined NSBL + LSND analysis

We now turn to a combined analysis of the NSBL and LSND results in  $(3 + 2)$  models, assuming statistical compatibility between the two datasets. The purpose of this combined analysis is to obtain the allowed regions in the mass parameter space  $(\Delta m^2_{41}, \Delta m^2_{51})$ , regardless of the simultaneous values for the mixing parameters. Results will be shown for  $\Delta m^2_{51} \geq \Delta m^2_{41}$ ; the case  $\Delta m^2_{41} > \Delta m^2_{51}$  can be obtained by simply interchanging  $\Delta m^2_{41}$  with  $\Delta m^2_{51}$ . The 95% CL allowed region is defined as the  $(\Delta m^2_{41}, \Delta m^2_{51})$  for which  $\chi^2_{\text{SBL}} - (\chi^2_{\text{SBL}})_{\text{min}} < 5.99$ , where  $(\chi^2_{\text{SBL}})_{\text{min}}$  is the absolute  $\chi^2$  minimum for all  $(\Delta m^2_{41}, \Delta m^2_{51})$  values. In the minimization procedure, the mixing matrix elements  $U_{e4}$ ,  $U_{\mu 4}$ ,  $U_{e5}$ ,  $U_{\mu 5}$ , are treated as free parameters.

Figure 7 shows the 90% and 99% CL allowed regions in  $(\Delta m^2_{41}, \Delta m^2_{51})$  space obtained in the combined  $(3 + 2)$  analysis. In light of the  $(3 + 1)$  analysis shown in previous sections, the result is not surprising, pointing to favored masses in the range  $\Delta m^2_{41} \approx 0.9 \text{ eV}^2$ ,  $\Delta m^2_{51} \approx$

$10 - 40 \text{ eV}^2$ , at 90% CL. At 99% CL, the allowed region extends considerably, and many other  $(\Delta m^2_{41}, \Delta m^2_{51})$  combinations appear. The best-fit model ( $\chi^2_{\text{SBL}} = 135.9$ , 145 d.o.f.) is described by the following set of parameters:  $\Delta m^2_{41} = 0.92 \text{ eV}^2$ ,  $U_{e4} = 0.121$ ,  $U_{\mu 4} = 0.204$ ,  $\Delta m^2_{51} =$

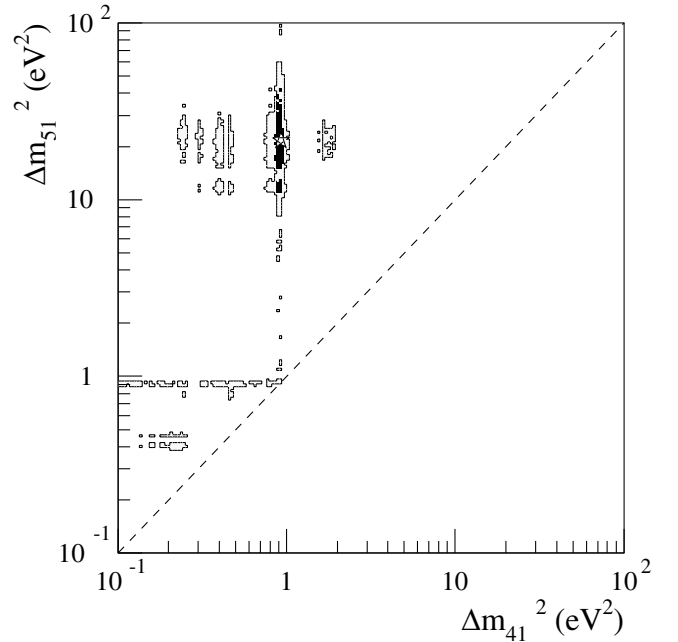


FIG. 7. Allowed ranges in  $(\Delta m^2_{41}, \Delta m^2_{51})$  space for  $(3 + 2)$  models, for the combined NSBL + LSND analysis, assuming statistical compatibility between the NSBL and LSND datasets. The star indicates the best-fit point, the dark and light gray-shaded regions indicate the 90 and 99% CL allowed regions, respectively. Only the  $\Delta m^2_{51} > \Delta m^2_{41}$  region is shown; the complementary region  $\Delta m^2_{41} \geq \Delta m^2_{51}$  can be obtained by interchanging  $\Delta m^2_{41}$  with  $\Delta m^2_{51}$ .

22 eV<sup>2</sup>,  $U_{e5} = 0.036$ , and  $U_{\mu5} = 0.224$ . We note here that the best fit is not obtained for fourth and fifth mass eigenstates with degenerate masses, that is for  $\Delta m_{41}^2 \simeq \Delta m_{51}^2$ . The best-fit model we found for sub-eV neutrino masses is  $\Delta m_{41}^2 = 0.46$  eV<sup>2</sup>,  $U_{e4} = 0.090$ ,  $U_{\mu4} = 0.226$ ,  $\Delta m_{51}^2 = 0.89$  eV<sup>2</sup>,  $U_{e5} = 0.125$ ,  $U_{\mu4} = 0.160$ , corresponding to  $\chi_{\text{SBL}}^2 = 141.5$  (145 d.o.f.).

## V. COMPARING THE (3 + 1) AND (3 + 2) FITS TO SBL DATA

In this section, we discuss four statistical tests that can be used to quantify the better overall agreement of SBL data to a (3 + 2) hypothesis for neutrino oscillations, compared to a (3 + 1) one.

### A. Test 1: NSBL upper limit on $p_{\text{LSND}}$ at a given confidence level $\delta_{\text{NSBL}}$

Test one uses only NSBL data to establish the (3 + 1) and (3 + 2) upper bounds on the LSND oscillation probability  $p_{\text{LSND}}$ . From Figs. 3 and 6, we obtain at a confidence level  $\delta_{\text{NSBL}} = 0.90(0.99)$ :

(i) (3 + 1):  $p_{\text{LSND}} < 0.100\%(0.162\%)$

(ii) (3 + 2):  $p_{\text{LSND}} < 0.186\%(0.262\%)$

Therefore, we find that (3 + 2) models can enhance the LSND probability  $p_{\text{LSND}}$  by quite a large factor, compared to (3 + 1) models. The increase in  $p_{\text{LSND}}$  that we obtain is significantly larger than the 25% increase found in [32], which is based on a specific choice of mixing parameters, as opposed to the complete parameter scan performed in this work. The value for the  $\bar{\nu}_\mu \rightarrow \bar{\nu}_e$  oscillation probability measured by LSND [6] is  $p_{\text{LSND}} = (0.264 \pm 0.067 \pm 0.045)\%$ , where the errors refer to the  $1\sigma$  statistical and systematic errors, respectively.

### B. Test 2: statistical compatibility between the NSBL and LSND datasets

Test two uses both the NSBL and LSND datasets, and treats them independently to find the combined confidence level  $\delta = \delta_{\text{NSBL}}[\delta_{\text{LSND}} + (1 - \delta_{\text{LSND}})/2]$  for which the datasets are incompatible, both in (3 + 1) and (3 + 2) models. The combined confidence levels can also be read from Figs. 3 and 6:

(i) (3 + 1):  $\delta = 96.4\%$

(ii) (3 + 2):  $\delta = 70.0\%$

Therefore, we find that in (3 + 1) models the two datasets are marginally compatible, and the agreement is better in (3 + 2) models.

### C. Test 3: likelihood ratio test

Test three combines the NSBL and LSND datasets into a single, joint analysis. The likelihood ratio test [35] provides a standard way to assess whether two hypotheses can be distinguished in a statistically significant way. We define the maximum likelihood  $\mathcal{L}_i$  from the minimum  $\chi^2$

values  $(\chi_{\text{SBL}}^2)_{\text{min},i}$  as  $\mathcal{L}_i \equiv \exp[-(\chi_{\text{SBL}}^2)_{\text{min},i}/2]$ , where the index  $i = 1, 2$  refers to the (3 + 1) and (3 + 2) hypotheses, respectively. We can then form the likelihood ratio  $\lambda_{1,2} \equiv \mathcal{L}_1/\mathcal{L}_2$ . If the (3 + 1) hypothesis were as adequate as the (3 + 2) hypothesis in describing SBL data, the quantity

$$\chi_{1,2}^2(3) \equiv -2 \ln \lambda_{1,2} = (\chi_{\text{SBL}}^2)_{\text{min},1} - (\chi_{\text{SBL}}^2)_{\text{min},2} \quad (9)$$

should be distributed as a  $\chi^2$  distribution with three degrees of freedom, where the number of degrees of freedom is the difference in the number of mass and mixing parameters in the (3 + 2) and (3 + 1) hypotheses,  $6 - 3 = 3$

In our combined fits, we obtain (see Sections III B and IV B):

(i) (3 + 1):  $(\chi_{\text{SBL}}^2)_{\text{min},1} = 144.9$ , (148 d.o.f.)

(ii) (3 + 2):  $(\chi_{\text{SBL}}^2)_{\text{min},2} = 135.9$ , (145 d.o.f.)

and therefore  $\chi_{1,2}^2(3) = 9.0$ . This value is significantly larger than three; the probability for a  $\chi^2$  distribution with 3 degrees of freedom to exceed the value 9.0 is only 2.9%. In other words, according to the likelihood ratio test, the (3 + 1) hypothesis should be rejected compared to the (3 + 2) one at the 97.1% CL. Therefore, based on this test, we conclude from test three also that (3 + 2) models fit SBL data significantly better than (3 + 1) models.

### D. Test 4: compatibility using the “parameter goodness of fit”

Test four uses both the results of the individual NSBL and LSND analyses, as well as the results of the combined NSBL + LSND analysis. The test is based on the “parameter goodness of fit” [36] to compare the compatibility of the NSBL and LSND results under the (3 + 1) and (3 + 2) hypotheses. The test avoids the problem that a possible disagreement between the two results is diluted by data points which are insensitive to the mass and mixing parameters that are common to both datasets. The number of parameters common to both datasets is  $P_c = 2$  in (3 + 1) models, and  $P_c = 4$  in (3 + 2) models. One possible choice of common parameters is  $(\Delta m_{41}^2, U_{e4}U_{\mu4})$  for (3 + 1) models,  $(\Delta m_{41}^2, U_{e4}U_{\mu4}, \Delta m_{51}^2, U_{e5}U_{\mu5})$  for (3 + 2) models. The test is based on the statistic  $\chi_{\text{PG}}^2 = \chi_{\text{PG,NSBL}}^2 + \chi_{\text{PG,LSND}}^2$ , where  $\chi_{\text{PG,NSBL}}^2 \equiv (\chi_{\text{NSBL}}^2)_{\text{SBLmin}} - (\chi_{\text{NSBL}}^2)_{\text{NSBLmin}}$  and  $\chi_{\text{PG,LSND}}^2 \equiv (\chi_{\text{LSND}}^2)_{\text{SBLmin}} - (\chi_{\text{LSND}}^2)_{\text{LSNDmin}}$  are the (positive) differences for the NSBL and LSND  $\chi^2$  values obtained by minimizing the entire SBL  $\chi^2$  function, minus the  $\chi^2$  values that best fit the individual datasets.

Table I gives the values for the parameter goodness of fit PG as defined in [36], based on the  $\chi_{\text{PG}}^2$  statistic, and the number of parameters common to the NSBL and LSND datasets,  $P_c$ . This test shows a dramatic improve-

TABLE I. Parameter goodness-of-fit PG, as defined in [36], to test the statistical compatibility between the NSBL and LSND datasets under the  $(3 + 1)$  and  $(3 + 2)$  hypotheses. The quantities  $\chi^2_{\text{PG,NSBL}}$  and  $\chi^2_{\text{PG,LSND}}$  are the NSBL and LSND contributions to the test statistic  $\chi^2_{\text{PG}}$  defined in the text;  $P_c$  indicates the number of parameters common to both datasets.

Model	$\chi^2_{\text{PG,NSBL}}$	$\chi^2_{\text{PG,LSND}}$	$\chi^2_{\text{PG}}$	$P_c$	PG (%)
$(3 + 1)$	11.8	4.3	16.1	2	$3.2 \cdot 10^{-2}$
$(3 + 2)$	7.1	4.4	11.5	4	2.1

ment in the compatibility between the NSBL and LSND results in going from a  $(3 + 1)$  to a  $(3 + 2)$  model, raising the compatibility by nearly 2 orders of magnitude, from 0.03% to 2.1%. It will be interesting to investigate if  $(3 + 3)$  models can improve the compatibility further. The resulting compatibility levels obtained with the parameter goodness-of-fit method are lower than those found in Sec. VB; this, however, is not surprising, since the two statistical tests are quite different.

## VI. ADDITIONAL CONSTRAINTS

The  $(3 + 1)$  and  $(3 + 2)$  models discussed in this work should be confronted with additional experimental constraints, other than the ones discussed in detail in the previous sections. We limit ourselves here to list and comment on some of these constraints, rather than address them in a quantitative way. Mostly, we will discuss the impact that such additional constraints may have on the best-fit  $(3 + 1)$  and  $(3 + 2)$  models found in Sections III and IV.

First, nonzero mixing matrix elements  $U_{e4}$ ,  $U_{\mu4}$ ,  $U_{e5}$ , and  $U_{\mu5}$  may cause observable effects in atmospheric neutrino data, in the form of zenith angle-independent suppressions of the  $\nu_\mu$  and  $\nu_e$  survival probabilities. Since our analysis of SBL data tends to give larger values for muon, rather than electron, flavor content in the fourth and fifth mass eigenstate, the effect should be larger on muon atmospheric neutrinos. For example, the  $(3 + 1)$  and  $(3 + 2)$  best-fit models from Sections III B and IV B would give an overall suppression of the  $\nu_\mu$  flux of 8% and 17%, respectively. The size of the effect of  $\nu_\mu \rightarrow \nu_x$  oscillations at high  $\Delta m^2$  is comparable to the current accuracy with which the absolute normalization of the atmospheric neutrino flux is known [37], which is approximately 20%. A more quantitative analysis using the full Super-Kamiokande and MACRO spectral information [27] puts an upper bound of 16% at 90% CL on this high  $\Delta m^2$  contribution to the atmospheric  $\nu_\mu$  flux suppression (in the notation of Ref. [27], this suppression is parametrized as  $2d_\mu(1 - d_\mu)$ , where  $d_\mu < 0.09$  at 90% CL). Therefore, it is expected that the inclusion of atmospheric neutrino data in this analysis would pull the best-fit muon flavor components in the fourth and fifth mass

eigenstates to lower values, but not in a dramatic way [see also Fig. 5(b)].

Second, models with large masses  $m_4$  and  $m_5$ , and with nonzero mixing matrix elements  $U_{e4}$  and  $U_{e5}$ , should be confronted with tritium  $\beta$  decay measurements. The presence of neutrino masses  $m_4$  and  $m_5$  introduces kinks in the differential  $\beta$  spectrum; the location in energy of the kinks is determined by the neutrino masses, and the size of the kinks is determined by the amount of electron flavor component in the fourth and fifth mass eigenstates. For a spectrometer integrating over the electron energy interval  $\delta$  near the  $\beta$  decay endpoint, the count rate is [38]

$$n(\delta) = \frac{\bar{R}}{3} \sum_{i=1}^n U_{ei}^2 (\delta^2 - m_i^2)^{3/2}, \quad (10)$$

where the quantity  $\bar{R}$  does not depend on the small neutrino masses and mixings,  $n = 4$  or  $n = 5$  for  $(3 + 1)$  or  $(3 + 2)$  models, respectively, and we have assumed  $\delta > m_i$ ,  $i = 1, \dots, n$ , and CP-invariance. From the experimental point of view, tritium  $\beta$  decay results are generally expressed in terms of a single effective mass  $m(\nu_e)$

$$n_s(\delta) = \frac{\bar{R}}{3} [\delta^2 - m(\nu_e)^2]^{3/2}, \quad (11)$$

where  $m(\nu_e)$  is the fit mass parameter. In the limit  $\delta^2 \gg m_i^2$ ,  $i = 1, \dots, n$  the relation between the true masses and mixings to the fitted mass  $m(\nu_e)$  is independent from the integration interval  $\delta$

$$m(\nu_e)^2 \simeq \sum_{i=1}^n U_{ei}^2 m_i^2. \quad (12)$$

The condition  $\delta^2 \gg m_i^2$ ,  $i = 1, \dots, n$  is generally satisfied for the neutrino masses considered in this paper, in order to ensure sufficient  $\beta$  decay count rate statistics in the experiments. Therefore, to a first approximation, we can consider the effect of heavy neutrino masses  $m_4$ ,  $m_5$  only on the single mass parameter  $m(\nu_e)$  fitted by the experiments. A more general analysis assessing the sensitivity of current and future  $\beta$  decay experiments to multiple fitted neutrino masses, although highly desirable, is beyond the scope of this work; for further details, the reader should consult Ref. [38]. The current best measurements on  $m(\nu_e)^2$  come from the Troitsk and Mainz experiments [39], which have very similar  $m(\nu_e)^2$  sensitivities. Both found no evidence for a nonzero  $m(\nu_e)^2$  value; the latest Mainz result is  $m(\nu_e)^2 = -1.6 \pm 2.5 \pm 2.1 \text{ eV}^2$ , or  $m(\nu_e) \leq 2.2 \text{ eV}$  at 95% CL, using  $\delta = 70 \text{ eV}$  [39]. Now, assuming a normal hierarchy ( $m_1 < m_4 < m_5$ ) with  $m_1 \simeq 0$ , the  $\beta$  decay neutrino mass in Eq. (12) can be written as  $m(\nu_e) \simeq U_{e4}^2 \Delta m_{41}^2 + U_{e5}^2 \Delta m_{51}^2$ ; the best-fit  $(3 + 1)$  and  $(3 + 2)$  models found in this analysis would give  $m(\nu_e)^2 = 0.017 \text{ eV}^2$  and  $m(\nu_e)^2 = 0.042 \text{ eV}^2$ , respectively, that is  $m(\nu_e)^2$  values



well below the current experimental sensitivity. The planned tritium  $\beta$  decay experiment KATRIN should be able to improve the sensitivity to  $m(\nu_e)$  by roughly an order of magnitude in the forthcoming years, thanks to its better statistics, energy resolution, and background rejection [40]. Specifically, the systematic and statistical (for  $\delta \gtrsim 30$  eV) uncertainties on the single fitted mass  $m(\nu_e)^2$  quoted for KATRIN are 0.018 and 0.016 eV<sup>2</sup>, respectively [40], which should provide some sensitivity to the preferred (3 + 1) and (3 + 2) neutrino models with a normal mass hierarchy,  $m_1 < m_4 < m_5$ . We now consider mass spectra with an inverted hierarchy, defined here as  $m_4 < m_1$  for (3 + 1) models, and  $m_5 < m_4 < m_1$  for (3 + 2) models. We note that for (3 + 2) models other hierarchies are also possible, but those do not satisfy the implicit assumption  $|\Delta m_{51}^2| = |\Delta m_{54}^2| + |\Delta m_{41}^2|$  taken in this analysis. The  $\beta$  decay neutrino mass in Eq. (12) can now be written as  $m(\nu_e)^2 \simeq |\Delta m_{41}^2|$  for inverted (3 + 1) models, and as  $m(\nu_e)^2 \simeq |\Delta m_{51}^2|$  for inverted (3 + 2) models. Clearly, in this case the  $\beta$  decay constraints depend strongly on the values of  $|\Delta m_{41}^2|$ ,  $|\Delta m_{51}^2|$ , and models with  $\gtrsim 5$  eV<sup>2</sup> mass splittings are already severely disfavored.

Third, introducing sterile neutrinos may affect a number of cosmological predictions, which are derived from various measurements [41]. The standard cosmological model predicts that sterile neutrinos in the  $\sim 1$  eV mass range with a significant mixing with active neutrinos would be present in the early Universe with the same abundance as the active neutrino species, in disagreement with cosmological observations [42,43]. On the other hand, several models have been proposed that would reconcile sterile neutrinos with cosmological observations, for example, suppressing thermal abundances for sterile neutrinos (see, *e.g.*, Ref.[42] and references therein). In particular, active-sterile oscillations in the early Universe may provide a natural mechanism to suppress the relic abundances of sterile neutrinos [44], and scenarios invoking multiple sterile neutrinos are being investigated [43].

## VII. CONCLUSIONS

We have performed a combined analysis of seven short-baseline experiments (Bugey, CHOOZ, CCFR84, CDHS, KARMEN, LSND, NOMAD) for both the (3 + 1) and the (3 + 2) neutrino oscillation hypotheses, involving one and two sterile neutrinos at high  $\Delta m^2$ , respectively. The motivation for considering more than one sterile neutrino arises from the tension in trying to reconcile, in a CPT-conserving, four-neutrino picture, the LSND signal for oscillations with the null results obtained by the other short-baseline experiments. Multiple (*e.g.* three) sterile neutrinos can also be motivated on theoretical grounds.

We have described two types of analyses for both the (3 + 1) and (3 + 2) neutrino oscillation hypotheses. In

the first analysis, we treat the LSND and the null short-baseline (NSBL) datasets separately, and we determine the statistical compatibility between the two. In the second analysis, we assume statistical compatibility and we combine the two datasets, to obtain the favored regions in neutrino mass and mixing parameter space.

The main results of the analysis are summarized in Sec. V, where we compare the adequacy of the (3 + 1) and (3 + 2) hypotheses in describing neutrino short-baseline data, by means of four statistical tests. First, we treat the LSND oscillation probability as a parameter that can be measured with NSBL data alone, and find that the NSBL 90% CL upper limit on the LSND oscillation probability can be significantly relaxed by going from (3 + 1) to (3 + 2) models, by about 80%. Second, the combined confidence level for which the NSBL and LSND datasets are incompatible is determined to be 96.4% and 70.0% in the analysis, for the (3 + 1) and (3 + 2) hypotheses, respectively. Third, a likelihood ratio test of the two hypotheses is discussed, and shows that the (3 + 1) hypothesis should be rejected compared to the (3 + 2) one at the 97.1% CL. Fourth, the parameter “goodness of fit” defined in [36] shows much better agreement between the NSBL and LSND results for (3 + 2) models than for (3 + 1) models.

In conclusion, we find that (3 + 1) models are only marginally allowed when considering all of the seven short-baseline results, including LSND, in agreement with previous analyses [32–34], and that (3 + 2) models can provide a better description of the data. Only the simplest neutrino mass and mixing patterns have been fully characterized in the literature so far, and the analysis described in this paper may be viewed as a simple attempt to explore more generic scenarios, which appear both experimentally and theoretically plausible. Given the bright potential for precision measurements by neutrino oscillation experiments in the near future, a more general phenomenological approach may be needed.

## ACKNOWLEDGMENTS

We thank J. Bouchez, L. Camilleri, K. Eitel, J. J. Gomez-Cadenas, E. A. Hawker, G. B. Mills, E. Nagy, V. Valuev, and G. P. Zeller for kindly providing data used in this analysis. We thank K. N. Abazajian, G. Barenboim, S. J. Brice, K. Eitel, B. Kayser, W. C. Louis, M. Maltoni, J. Monroe, P. Nienaber, T. Schwetz, A. Y. Smirnov, and K. Whisnant for valuable discussions and useful suggestions. This work was supported by NSF.

## APPENDIX: PHYSICS AND STATISTICAL ASSUMPTIONS

In this section, we briefly describe the physics and statistical assumptions used to obtain the approximate characterizations of the short-baseline experiments used in the analysis. For the analysis of the Bugey, CDHS, and

KARMEN data, we also refer to the excellent reference [34], which we followed closely.

The Bugey experiment [18] is sensitive to  $\bar{\nu}_e$  disappearance by measuring the charged-current interaction of  $\bar{\nu}_e$ 's produced by two nuclear reactors at the Bugey nuclear power plant. Two liquid scintillator detectors, located at different positions, are used. The signature for an antineutrino interaction is a positron and a delayed light pulse produced by the subsequent neutron capture on  ${}^6\text{Li}$ . Data are given for three baselines: 15, 40, and 95 m between neutrino production and detection. We follow the “normalized energy spectra” analysis discussed in the Bugey paper [18]. The data are presented as ratios of observed to predicted (for no-oscillations) positron energy spectra, between one and 6 MeV positron energy. We use 25, 25, and ten positron energy bins for the 15, 40, 95 m baselines, respectively. In the  $\chi^2$  analysis, fits included not only the mass and mixing parameters, but also five large scale deformations of the positron spectrum due to systematic effects. The experimental positron energy resolution and the neutrino baseline smearing are taken into account; the neutrino cross-section energy dependence within a positron energy bin is not (the energy bin widths are small).

Similarly, the CHOOZ experiment [21] investigates  $\bar{\nu}_e$  disappearance by observing interactions of  $\bar{\nu}_e$ 's produced by two nuclear reactors  $\approx 1$  km away from the CHOOZ detector. The signature for a neutrino interaction is a delayed coincidence between the prompt  $e^+$  signal and the signal due to the neutron capture in the Gd-loaded scintillator. We follow “analysis A,” as discussed in the CHOOZ paper [21]. Data are given as positron yields as a function of energy. In this analysis, seven positron energy bins, between 0.8 and 6.4 MeV, are considered, for which the CHOOZ observations, as well as the predictions on the positron yields for the no-oscillation case from both reactors, are given in [21]. Because of the presence of two reactor sources, the  $\chi^2$  analysis comprises 14 positron yield bins for a given energy/baseline. We use the full covariance matrix to take into account the fact that the yields corresponding to the same energy bin are extracted for both reactors simultaneously, as is done in [21]. The analysis fits for the systematic uncertainty in the absolute normalization constant on the  $\bar{\nu}_e$  yield from the reactors, in addition to the mass and mixing parameters. Since we are interested in the  $\Delta m^2 > 0.1$  eV<sup>2</sup> range only, where no energy shape distortions are expected, we neglect the systematic uncertainty on the energy-scale calibration, and the effect of the positron energy resolution.

The CCFR84 experiment [19] constrains  $\nu_\mu$  and  $\bar{\nu}_\mu$  disappearance by measuring the charged-current interaction of muon neutrinos and antineutrinos, produced by a Fermilab secondary, sign selected beam yielding  $40 < E_\nu < 230$  GeV neutrinos from  $\pi^\pm$  and  $K^\pm$  decays in the 352 m long decay pipe. We refer here to the 1984 CCFR

experiment (hence the label CCFR84 throughout the text), which operated with two similar detectors located at different distances from the neutrino source, 715 and 1116 m from the midpoint of the decay region, respectively. The two sampling calorimeter detectors consisted of steel plates and scintillation counters. Six secondary beam momentum settings were used, five for neutrino running, and one for antineutrino running. For each secondary beam momentum setting, the data are divided into three neutrino energy bins, for a total of 18 energy bins, from Ref.[45]. Data are presented as double ratios: the far to near detector ratio of observed number of events, divided by the far to near ratio of events predicted for no-oscillations. As in [19], only the mean neutrino energy for a given neutrino energy bin is used in the  $\chi^2$  analysis. The systematic and statistical uncertainties on the far to near ratio normalization are taken into account. The systematic uncertainty is assumed to be energy-independent and totally correlated between any two energy bins. The neutrino pathlength smearing, mostly due to the long decay region, is also taken into account.

The CDHS experiment [20] is also sensitive to  $\nu_\mu$  disappearance via the charged-current interaction of  $\nu_\mu$ 's, produced by a 19.2 GeV/c proton beam from the CERN Proton Synchrotron. Two detectors are located at 130 and 835 m from the target. The detectors are sampling calorimeters, with iron and scintillator modules interspersed, to measure the range of a muon produced in a neutrino interaction. Fifteen muon range bins are used. The data are presented as double ratios: the far to near detector ratio of the observed number of events, divided by the far to near ratio of the number of events predicted for no oscillations. Neutrino energy distributions are obtained for a given muon energy (or range) via the NUANCE [46] neutrino cross-section generator. As for CCFR84, the systematic uncertainty on the far to near ratio and the neutrino baseline smearing are taken into account.

The KARMEN experiment [22] investigates the  $\bar{\nu}_\mu \rightarrow \bar{\nu}_e$  appearance channel, from  $\bar{\nu}_\mu$ 's produced in the  $\pi^+ \mu^+$ -decay at rest (DAR) chain of the ISIS neutrino source. KARMEN measures the charged-current interaction  $p(\bar{\nu}_e, e^+)n$ , with a liquid scintillator detector located at an average distance 17.7 m downstream of the neutrino source. The  $\bar{\nu}_e$  signature is a spatially correlated delayed coincidence between a prompt positron and a delayed  $\gamma$  event from a  $(n, \gamma)$  neutron capture reaction. In this analysis, only the positron (“prompt”) energy distribution after all cuts is taken into account, given in [22]. The data are binned into nine prompt energy bins, between 16 and 50 MeV (all bins are 4 MeV wide, except the highest energy one, ranging from 48 to 50 MeV). In predicting the prompt energy distribution for a set of mass and mixing oscillation parameters, the given Monte Carlo positron energy distribution, and the total number of events ex-

pected after all cuts for full mixing and  $\Delta m^2 = 100 \text{ eV}^2$ , are used [47]. Energy resolution and baseline smearing effects (due to finite detector size) are taken into account. Given the low statistics of the nine KARMEN prompt energy bins, we construct the  $\chi^2$  function by first defining the likelihood ratio [25]

$$\lambda(\theta) = \frac{f[\mathbf{n}; \boldsymbol{\mu}(\theta), \mathbf{b}]}{f(\mathbf{n}; \mathbf{n}, \mathbf{b})}, \quad (\text{A1})$$

where  $\theta$  denotes schematically all mass and mixing parameters,  $\mathbf{n}$ ,  $\boldsymbol{\mu}(\theta)$  and  $\mathbf{b}$  are the data, expected signal, and expected background vectors with nine elements, and  $f[\mathbf{n}; \boldsymbol{\mu}(\theta), \mathbf{b}]$  are the probabilities for a Poisson process with known background

$$f[\mathbf{n}; \boldsymbol{\mu}(\theta), \mathbf{b}] = \prod_{i=1}^9 \frac{(\mu_i + b_i)^{n_i} \exp[-(\mu_i + b_i)]}{n_i!} \quad (\text{A2})$$

We define  $\chi_{\text{KARMEN}}^2$  as

$$\chi_{\text{KARMEN}}^2 \equiv -2 \ln \lambda(\theta). \quad (15)$$

The LSND experiment at Los Alamos [6] is also sensitive to  $\bar{\nu}_\mu \rightarrow \bar{\nu}_e$  appearance, with a neutrino source and detection signature similar to that of KARMEN, but with better statistics. The LSND liquid scintillator detector is located at an average distance of 30 m from the neutrino source. As for KARMEN, in this analysis we consider only the positron energy distribution arising from a  $\bar{\nu}_e$  interaction in mineral oil, published as five energy bins between 20 and 60 MeV [6]. Our analysis ignores the information arising from the higher-energy neutrinos from pions decaying in flight, which has a smaller (but non-negligible) sensitivity to oscillations compared to the decay at rest (DAR) sample considered here. In our simulation, we take into account the expected energy distribution from  $\mu^+$  decay at rest, the neutrino baseline distribution for the 8 m long cylindrical detector, the neutrino energy dependence of the cross-section for the detection process  $p(\bar{\nu}_e, e^+)n$  (including nuclear effects, simulated with the NUANCE [46] neutrino cross-section generator), and the experimental energy resolution. We use the published numbers for the background expectations, the number of  $\bar{\nu}_e$  events for 100%  $\bar{\nu}_\mu \rightarrow \bar{\nu}_e$  transmutation, and for the efficiency of the event selection criteria. We construct the LSND  $\chi^2$  function in the same way as we construct the one for KARMEN, because of the low statistics of the data sample.

Finally, the NOMAD experiment is sensitive to  $\nu_\mu \rightarrow \nu_e$  oscillations at  $\Delta m^2 \gtrsim 1 \text{ eV}^2$  by looking for charged-current muon neutrino and electron neutrino interactions in the NOMAD detector [23]. The detector consists of a large dipole magnet which houses drift chambers to measure the momenta of the charged particles produced

in neutrino interactions; transition radiation modules for lepton identification; an electromagnetic calorimeter to measure the energy of electrons and photons; a hadron calorimeter for particle identification; and muon chambers for muon identification. Neutrinos are produced by impinging 450 GeV protons extracted from the CERN SPS accelerator onto a thick beryllium target. The secondary particles produced in the target are focused into a nearly parallel beam by two magnetic lenses, and decay in a 290 m long decay tunnel to produce a  $\sim 10 - 100 \text{ GeV}$  neutrino beam with about 1%  $\nu_e$  contamination. Neutrino interactions are then observed in the NOMAD detector at an average distance of 625 m from the neutrino source. The  $\nu_\mu \rightarrow \nu_e$  search is performed by comparing the measured ratio  $R_{e\mu}$  of the number of  $\nu_e$  to  $\nu_\mu$  charged-current neutrino interactions with the one expected in the absence of oscillations. The data are binned into 30 bins, covering ten bins in visible energy between three and 170 GeV, and three radial bins in the neutrino interaction vertex. A  $\chi^2$  analysis is performed, using the final NOMAD numbers on the observed and predicted electron-to-muon ratio, including statistical errors as well as the full error matrix describing systematic uncertainties and uncertainty correlations over different bins [48]. In predicting the effect of  $\nu_\mu \rightarrow \nu_e$  oscillations under any mass and mixing hypothesis, the contribution to  $R_{e\mu}$  from oscillations with full mixing and  $\Delta m^2 = 5000 \text{ eV}^2$  expected in NOMAD after all cuts are used [48]. Energy resolution and baseline smearing effects (due to the long decay region) are taken into account [23].

In Fig. 8, we show our calculations of the 90% CL upper limits on oscillations as a function of  $\Delta m^2$  for the six NSBL experiments considered here, as well as the 90% CL allowed region for LSND. The  $(\chi^2)_{\min}$  values as a function of  $\Delta m^2$  for all of the experiments are also shown. All the solid curves shown are obtained from the simplified analysis described here, and compare well with the published results [6,18–23].

The LSND region obtained in our analysis of DAR neutrinos is slightly shifted to the right compared to the final LSND area, shown in Fig. 8(f) as a dashed line, reflecting the difference in the two datasets. More detailed LSND DAR analyses give results in rough agreement with our allowed region [12,30].

The  $(\chi^2)_{\min}$  values obtained for the Bugey and CDHS experiments as a function of  $\Delta m^2$  give details that might seem surprising, at first. Slightly better fits to the data are obtained under a neutrino oscillations hypothesis, as opposed to the no-oscillations one. Therefore, we add a final comment to explain the results of these fits.

The Bugey fit is driven by the data at the shortest baseline, 15 m, where the statistical errors on the observed positron spectrum from  $\bar{\nu}_e$  interactions are the smallest. As explained in Ref.[18], systematic uncertainties are taken into account by allowing for linear defor-

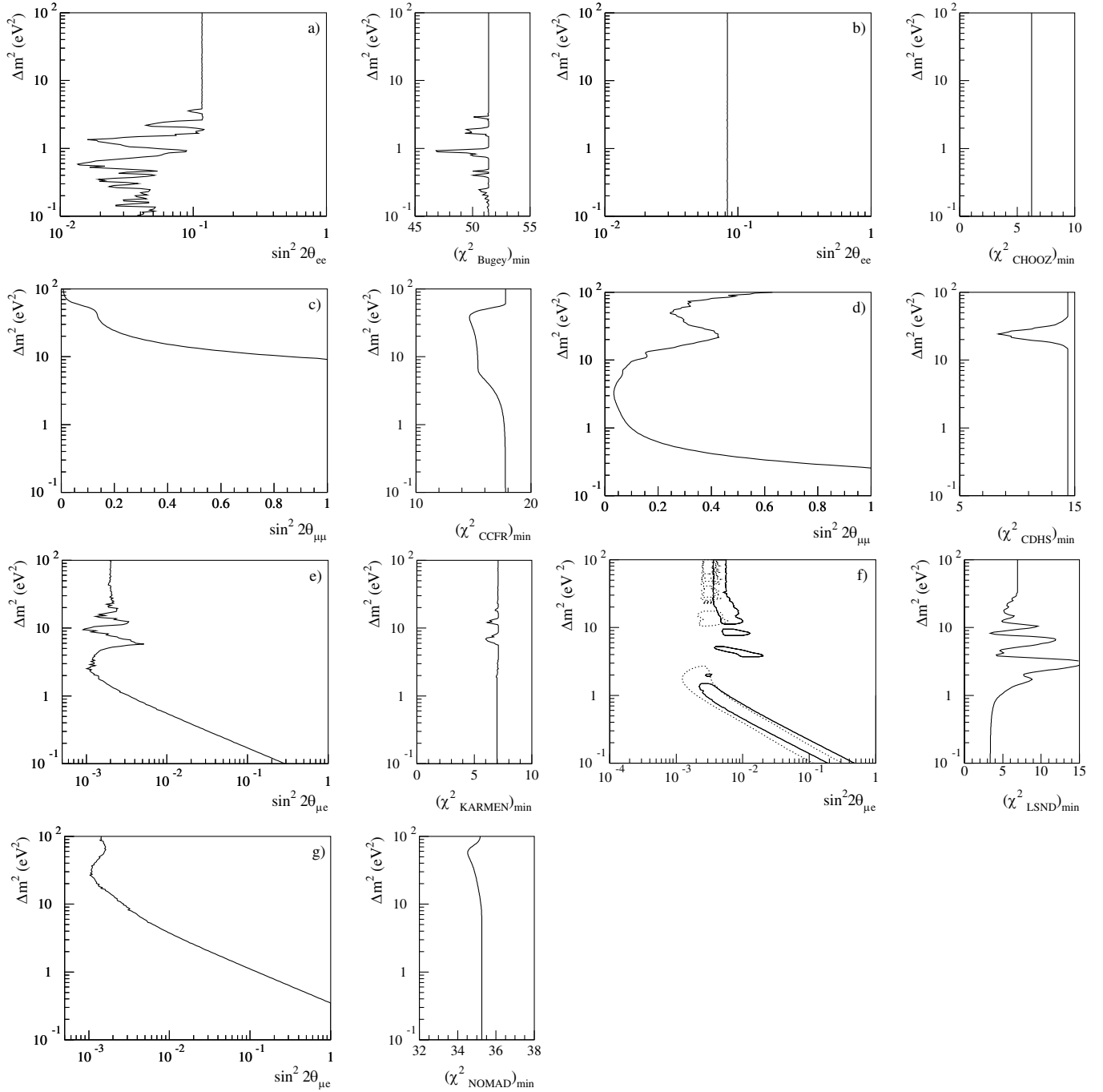


FIG. 8. 90% CL upper limits on oscillations derived in this analysis for the following NSBL experiments: (a) Bugey, (b) CHOOZ, (c) CCFR84, (d) CDHS, (e) KARMEN, (g) NOMAD. Figure (f) shows the LSND 90% CL allowed region obtained with the decay-at-rest analysis described in the Appendix (solid line), superimposed to the published LSND 90% CL allowed region (dashed line). Also shown are the  $(\chi^2)_{\min}$  values as a function of  $\Delta m^2$  obtained by all the experiments considered individually. The number of degrees of freedom is 58 in Bugey, 12 in CHOOZ, 16 in CCFR84, 13 in CDHS, seven in KARMEN, three in LSND, 28 in NOMAD.

mations, as a function of positron energy, of the ratio of observed to predicted positron yields. The values of  $(\chi^2_{\text{Bugey}})_{\min}$  as a function of  $\Delta m^2$  are explained by the fact that, for certain  $\Delta m^2$  values, an oscillatory fit to the 15 m positron spectrum ratio describes the data marginally better than any straight line. Our best-fit oscillation

hypothesis to Bugey data only is  $\Delta m^2 = 0.92 \text{ eV}^2$ ,  $\sin^2 2\theta_{ee} = 0.05$ .

For CDHS, the  $(\chi^2_{\text{CDHS}})_{\min}$  curve in Fig. 8(d) has a minimum at  $\Delta m^2 \approx 20 - 30 \text{ eV}^2$ . This minimum is due to the fact that the far/near  $\nu_\mu$  rate ratio, corrected for the baseline and detector mass differences between the two

detectors (as well as other minor effects), is measured to be slightly greater than one [20]:  $R_{\text{corr}} = 1.044 \pm 0.023 \pm 0.025$ . This marginal deviation from one causes the fit procedure to prefer more  $\nu_\mu$  disappearance by oscillations in the near than in the far detector. Given the

average  $\nu_\mu$  energy (3.2 GeV) and pathlength (130 m) for neutrinos interacting in the CDHS near detector, this condition is satisfied in the  $\Delta m^2 = 20 - 30 \text{ eV}^2$  range. Our best-fit oscillation hypothesis to CDHS data only is  $\Delta m^2 = 24 \text{ eV}^2$ ,  $\sin^2 2\theta_{\mu\mu} = 0.29$ .

- 
- [1] Kamiokande Collaboration, Y. Fukuda *et al.*, Phys. Lett. **B335**, 237 (1994); R. Becker-Szendy *et al.*, Nucl. Phys. B, Proc. Suppl. **38**, 331 (1995); Soudan-2 Collaboration, W.W. Allison *et al.*, Phys. Lett. **B449**, 137 (1999).
  - [2] Super-Kamiokande Collaboration, Y. Fukuda *et al.*, Phys. Rev. Lett. **81**, 1562 (1998).
  - [3] MACRO Collaboration, M. Ambrosio *et al.*, Phys. Lett. **B517**, 59 (2001).
  - [4] B.T. Cleveland *et al.*, Astrophys. J. **496**, 505 (1998); GALLEX Collaboration, P. Anselmann *et al.* Phys. Lett. **B285**, 376 (1992); D.N. Abdurashitov *et al.*, Phys. Lett. **B328**, 234 (1994).
  - [5] SNO Collaboration, Q.R. Ahmad *et al.*, Phys. Rev. Lett. **87**, 071301 (2001); SNO Collaboration, Q.R. Ahmad *et al.*, Phys. Rev. Lett. **89**, 011301 (2002); Super-Kamiokande Collaboration S. Fukuda *et al.*, Phys. Lett. **B539**, 179 (2002).
  - [6] LSND Collaboration, C. Athanassopoulos *et al.*, Phys. Rev. Lett. **77**, 3082 (1996); LSND Collaboration, C. Athanassopoulos *et al.*, Phys. Rev. C **58**, 2489 (1998); LSND Collaboration A. Aguilar *et al.*, Phys. Rev. D **64**, 112007 (2001).
  - [7] BooNE Collaboration, A. O. Bazarko, hep-ex/9906003.
  - [8] M. Maltoni, T. Schwetz, and J.W.F. Valle, Phys. Rev. D **65**, 093004 (2002).
  - [9] C. Giunti, M.C. Gonzalez-Garcia and C. Peña-Garay, Phys. Rev. D **62**, 013005 (2000).
  - [10] G. Barenboim and F. Scheck, Phys. Lett. **B440**, 332 (1998); G. Barenboim, A. Dighe, and S. Skadhauge, Phys. Rev. D **65**, 053001 (2002).
  - [11] H. Murayama and T. Yanagida, Phys. Lett. **B520**, 263 (2001); G. Barenboim, L. Borisso, J. Lykken, and A.Y. Smirnov, J. High Energy Phys. **0210**, 001 (2002); G. Barenboim, L. Borisso, and J. Lykken, hep-ph/0212116.
  - [12] M. Maltoni, T. Schwetz, M. A. Tortola, and J.W.F. Valle, Nucl. Phys. **B643**, 321 (2002).
  - [13] H. Paes, L. Song, and T. J. Weiler, Phys. Rev. D **67**, 073019 (2003).
  - [14] P. Ramond, hep-ph/9809459.
  - [15] R. N. Mohapatra and R. E. Marshak, Phys. Rev. Lett. **44**, 1316 (1980); *ibid.* **44**, 1643(E) (1980).
  - [16] R. R. Volkas, Prog. Part. Nucl. Phys. **48**, 161 (2002).
  - [17] G. J. Stephenson, T. Goldman, B. H. J. McKellar, and M. Garbutt, hep-ph/0307245; K. S. Babu and G. Seidl, Phys. Lett. **B591**, 127 (2004); K. L. McDonald, B. H. J. McKellar, and A. Mastrano, hep-ph/0401241.
  - [18] Y. Declais *et al.*, Nucl. Phys. **B434**, 503 (1995).
  - [19] I. E. Stockdale *et al.*, Phys. Rev. Lett. **52**, 1384 (1984).
  - [20] F. Dydak *et al.*, Phys. Lett. B **134**, 281 (1984).
  - [21] M. Apollonio *et al.*, Eur. Phys. J. C **27**, 331 (2003).
  - [22] KARMEN Collaboration, B. Armbruster *et al.*, Phys. Rev. D **65**, 112001 (2002).
  - [23] NOMAD Collaboration, P. Astier *et al.*, Phys. Lett. **B570**, 19 (2003); D. Gibin, Nucl. Phys. B, Proc. Suppl. **66**, 366 (1998); NOMAD Collaboration, V. Valuev, in *International Europhysics Conference on High-Energy Physics (JHEP), Budapest, 2001* [J. High Energy Phys. Conf. Proc., PRHEP-hep2001/190 (2001)].
  - [24] B. Kayser, hep-ph/0211134.
  - [25] Particle Data Group Collaboration, K. Hagiwara *et al.*, Phys. Rev. D **66**, 010001 (2002).
  - [26] S. M. Bilenky, C. Giunti, W. Grimus, and T. Schwetz, Phys. Rev. D **60**, 073007 (1999).
  - [27] M. Maltoni, T. Schwetz, and J.W.F. Valle, Phys. Lett. **B518**, 252 (2001).
  - [28] F. James and M. Roos, Comput. Phys. Commun. **10**, 343 (1975).
  - [29] G. J. Feldman and R. D. Cousins, Phys. Rev. D **57**, 3873 (1998).
  - [30] E. D. Church, K. Eitel, G. B. Mills, and M. Steidl, Phys. Rev. D **66**, 013001 (2002).
  - [31] K. Eitel, New J. Phys. **2**, 1 (2000).
  - [32] O. L. G. Peres and A. Y. Smirnov, Nucl. Phys. **B599**, 3 (2001).
  - [33] A. Strumia, Phys. Lett. **B539**, 91 (2002).
  - [34] W. Grimus and T. Schwetz, Eur. Phys. J. C **20**, 1 (2001).
  - [35] W. T. Eadie, D. Drijard, F. E. James, M. Roos, B. Sadoulet, *Statistical Methods in Experimental Physics* (North Holland, Amsterdam, 1971).
  - [36] M. Maltoni and T. Schwetz, Phys. Rev. D **68**, 033020 (2003); M. Maltoni, T. Schwetz, M. A. Tortola, and J.W.F. Valle, Phys. Rev. D **68**, 003020 (2003).
  - [37] M. Honda, T. Kajita, K. Kasahara, and S. Midorikawa, Phys. Rev. D **52**, 4985 (1995); Y. Liu, L. Derome, and M. Buenerd, Phys. Rev. D **67**, 073022 (2003).
  - [38] Y. Farzan and A. Y. Smirnov, Phys. Lett. **B557**, 224 (2003); Y. Farzan, O. L. G. Peres, and A. Y. Smirnov, Nucl. Phys. **B612**, 59 (2001).
  - [39] V. M. Lobashev *et al.*, Nucl. Phys. B, Proc. Suppl. **91**, 280 (2001); J. Bonn *et al.*, Nucl. Phys. B, Proc. Suppl. **91**, 273 (2001).
  - [40] KATRIN Collaboration, A. Osipowicz *et al.*, hep-ex/0109033; KATRIN Collaboration, L. Bornschein *et al.* in *Proceeding of the 23rd International Conference on Physics in Collision, Zeuthen, Germany, 2003*, eConf C030626, FRAP14 (2003).

- [41] D. N. Spergel *et al.*, *Astrophys. J. Suppl. Ser.* **148**, 175 (2003); W. J. Percival *et al.*, *Mon. Not. R. Astron. Soc.* **327**, 1297 (2001); J. M. O'Meara, D. Tytler, D. Kirkman, N. Suzuki, J. X. Prochaska, D. Lubin, and A. M. Wolfe, *Astrophys. J.* **552**, 718 (2001); W. L. Freedman *et al.*, *Astrophys. J.* **553**, 47 (2001).
- [42] K. N. Abazajian, *Astropart. Phys.* **19**, 303 (2003).
- [43] P. Di Bari, *Phys. Rev. D* **67**, 127301 (2003); P. Di Bari, *Phys. Rev. D* **65**, 043509 (2002).
- [44] R. Foot, M. J. Thomson, and R. R. Volkas, *Phys. Rev. D* **53**, 5349 (1996).
- [45] I. E. Stockdale, FERMILAB Report No. FERMILAB-THESIS-1984-08, 1984 (unpublished).
- [46] D. Casper, *Nucl. Phys. B, Proc. Suppl.* **112**, 161 (2002).
- [47] KARMEN collaboration, K. Eitel *et al.*, **77**, 212 (1999).
- [48] V. Valuev, (private communication).

## 2.3 Short-baseline neutrino experiments and leptonic CP-violation

One of the most pressing open questions in neutrino physics today is whether or not leptons, like baryons, do not conserve the fundamental CP symmetry. The consequences of a leptonic CP symmetry violation would be far-reaching and extend beyond the realm of particle physics, possibly being related to the matter-antimatter asymmetry observed in the Universe today.

In the standard paradigm of three active neutrino mixing occurring at the solar and atmospheric oscillation scales only, leptonic CP violation would yield different vacuum oscillation probabilities for neutrinos and antineutrinos that could be observed with accelerator-based neutrino oscillation appearance experiments operating near the atmospheric oscillation maximum. This is because CP-odd terms in the oscillation probability formula would appear from solar/atmospheric interference terms involving the single CP-violating Dirac phase appearing in the neutrino mixing matrix. An ambitious experimental program is currently being planned to try to measure this CP-violating phase.

Neutrino models involving active/sterile neutrino mixing at the LSND neutrino mass splitting scale via at least two sterile neutrino states would open the possibility for further manifestations of leptonic CP violation, including ones that could be measurable with neutrino appearance experiments at short baselines also. In the following, short-baseline leptonic CP-violation in  $(3+2)$  sterile neutrino models is discussed, based on work done in collaboration with A. Aguilar-Arevalo, V. Barger, J. Conrad, M. Shaevitz, and K. Whisnant [3]. The first main result of this work is that a combined analysis of current short-baseline oscillation results allow for all possible values for the CP-violating phase that could be measurable at short baselines. The second main result is that CP violation at short baselines could significantly alter the expectations for oscillations in MiniBooNE neutrino running mode, based on



the LSND antineutrino oscillation signal indication. In this scenario, an additional MiniBooNE antineutrino run would be highly desirable. Third,, the studies show that the combination of high-statistics MiniBooNE  $\nu_\mu \rightarrow \nu_e$  and  $\bar{\nu}_\mu \rightarrow \bar{\nu}_e$  searches could, under favorable circumstances, lead to the measurement of this short-baseline CP-violating phase.

### 2.3.1 Neutrino oscillation formalism

For  $N$  neutrino species, the general neutrino oscillation formula is:

$$P(\nu_\alpha \rightarrow \nu_\beta) = \delta_{\alpha\beta} - \sum_{i < j} (4\text{Re}[U_{\beta j} U_{\alpha j}^* U_{\beta i}^* U_{\alpha i}] \sin^2 x_{ji} - 2\text{Im}[U_{\beta j} U_{\alpha j}^* U_{\beta i}^* U_{\alpha i}] \sin 2x_{ji}) \quad (2.1)$$

where  $\alpha, \beta \equiv e, \mu, \tau$ , or sterile flavor,  $i, j = 1, \dots, N$ ,  $x_{ji} \equiv 1.27 \Delta m_{ji}^2 L/E$ , the neutrino mass splitting  $\Delta m_{ji}^2 \equiv m_j^2 - m_i^2$  is in  $\text{eV}^2$ , the neutrino baseline  $L$  in km, and the neutrino energy  $E$  is in GeV. Therefore, there are, in general,  $(N - 1)$  independent mass splittings,  $N - N(N - 1)/2$  independent moduli of parameters in the unitary mixing matrix, and  $(N - 1)(N - 2)/2$  CP-violating phases that may be observed in oscillations.

In short-baseline neutrino experiments that are sensitive only to  $\nu_\mu \rightarrow \nu_\mu$ ,  $\nu_e \rightarrow \nu_e$ , and  $\nu_\mu \rightarrow \nu_e$  transitions, the set of observable parameters simplifies considerably. First, oscillations due to atmospheric and solar mass splittings can be neglected in this case, or equivalently one can set  $m_1 = m_2 = m_3$ . Second, mixing matrix elements that measure the  $\tau$  neutrino flavor fraction of the various neutrino mass eigenstates do not enter in the oscillation probability. In this case, the number of observable parameters restricts to  $(N - 3)$  independent mass splittings,  $2(N - 3)$  moduli of mixing matrix parameters, and  $(N - 3)(N - 4)/2$  CP-violating phases. Therefore, for (3+2) sterile neutrino models depicted in Fig. 2.1, there are two independent mass splittings  $\Delta m_{41}^2$  and  $\Delta m_{51}^2$ , four moduli of mixing matrix parameters  $|U_{e4}|$ ,  $|U_{\mu 4}|$ ,  $|U_{e5}|$ ,  $|U_{\mu 5}|$ , and one CP-violating phase. The convention used in the following for this CP-phase

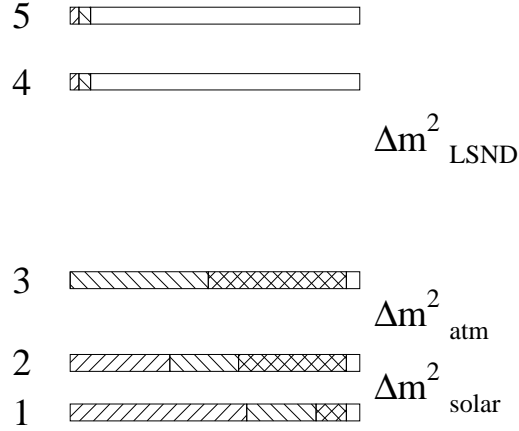


Figure 2.1: *Flavor content of neutrino mass eigenstates in (3+2) models. Neutrino masses increase from bottom to top. The  $\nu_e$  fractions are indicated by right-leaning hatches, the  $\nu_\mu$  fractions by left-leaning hatches, the  $\nu_\tau$  fractions by crosshatches, and the  $\nu_s$  fractions by no hatches. The flavor contents shown are schematic only.*

is:

$$\phi_{54} = \arg(U_{e5}U_{\mu5}^*U_{e4}^*U_{\mu4}) \quad (2.2)$$

Under these assumptions, the general oscillation formula in Eq. 2.1 can be rewritten as:

$$P(\nu_\alpha \rightarrow \nu_\alpha) = 1 - 4(1 - |U_{\alpha4}|^2 - |U_{\alpha5}|^2) + (|U_{\alpha4}|^2 \sin^2 x_{41} + |U_{\alpha5}|^2 \sin^2 x_{51}) + |U_{\alpha4}|^2 |U_{\alpha5}|^2 \sin^2 x_{54} \quad (2.3)$$

$$P(\nu_\alpha \rightarrow \nu_\beta) = 4|U_{\alpha4}|^2 |U_{\beta4}|^2 \sin^2 x_{41} + 4|U_{\alpha5}|^2 |U_{\beta5}|^2 \sin^2 x_{51} + 8|U_{\alpha5}| |U_{\beta5}| |U_{\alpha4}| |U_{\beta4}| \sin x_{41} \sin x_{51} \cos(x_{54} + \phi_{54}) \quad (2.4)$$

for  $\alpha = \beta$  and  $\alpha \neq \beta$ , respectively. The formulas for antineutrino oscillations are obtained by substituting  $\phi_{54} \rightarrow -\phi_{54}$ .

### 2.3.2 Analysis method

The analysis method used for CP violation studies at short baselines uses similar tools to the ones described in [2], plus a realistic simulation of the MiniBooNE sensitivity to  $\bar{\nu}_{\mu} \rightarrow \bar{\nu}_e$  oscillations, in both neutrino and antineutrino running modes.

#### Parameter estimation via Monte Carlo techniques

The analysis uses the same seven short-baseline datasets on  $\nu_{\mu}$  disappearance (from the CCFR84 and CDHS experiments),  $\nu_e$  disappearance (from the Bugey and CHOOZ experiments), and  $\nu_{\mu} \rightarrow \nu_e$  oscillations (from the LSND, KARMEN2, and NOMAD experiments) as in Ref. [2] to estimate the range of fundamental neutrino parameters in (3+2) models that are experimentally allowed. However, in this case, CP-violating values for the phase  $\phi_{54}$  from Eq. 2.2 are also considered, allowing for different neutrino and antineutrino oscillation probabilities in Eq. 2.4.

The Monte Carlo method used in the analysis to estimate the regions in neutrino parameter space that are experimentally allowed by short-baseline results is very similar to the one described in Ref. [2]. Slight modifications to this method have been applied in this case, mainly because of the larger dimensionality of the parameter set present in CP-violating models compared to CP-conserving ones. Rather than generating neutrino masses and mixings in a random, unbiased, way, importance sampling via a Markov chain Monte Carlo method is used [4, 5], to better sample the regions in parameter space that provide a good fit to short-baseline data. Given a starting point (model)  $x_i$  in the  $(\Delta m_{41}^2, |U_{e4}|, |U_{\mu 4}|, \Delta m_{51}^2, |U_{e5}|, |U_{\mu 5}|, \phi_{54})$  parameters space, a trial state  $x_{i+1} = x_i + e$  that depends only on the current state  $x_i$  and on the probability distribution function for the random vector  $e$  is generated. The probability for the trial state  $x_{i+1}$  to be accepted as the new current state for further model random generation is given by the transition probability:

$$P(x_i \rightarrow x_{i+1}) = \min\{1, \exp[-(\chi_{i+1}^2 - \chi_i^2)/T]\} \quad (2.5)$$

where  $\chi_i^2$  and  $\chi_{i+1}^2$  are  $\chi^2$  values for the states  $x_i$  and  $x_{i+1}$ , quantifying the agreement between the models and the short-baseline results used in the combined analysis, and  $T$  is an effective “temperature” parameter. The results presented here are obtained by combining various Markov chains with different initial conditions, probability distribution functions for  $e$ , and temperature parameters.

### MiniBooNE sensitivity

This analysis also provides realistic estimates of the sensitivity to  $\bar{\nu}_\mu \rightarrow \bar{\nu}_e$  oscillations that can be achieved with the MiniBooNE experiment, in the framework of CP-conserving and CP-violating (3+2) sterile neutrino models that are currently allowed.

The MiniBooNE sensitivity to (3+2) sterile neutrino oscillations is computed using the full MiniBooNE simulations for neutrino fluxes, neutrino cross-sections, event reconstruction and particle identification in the detector, as done in the MiniBooNE Run Plan [6]. The analysis includes the expected neutrino statistics for  $10^{21}$  protons on target in both neutrino and antineutrino running mode, background levels to the  $\nu_e/\bar{\nu}_e$  appearance searches from particle misidentification and intrinsic  $\nu_e$ ’s in the beam, systematic uncertainties associated with those backgrounds, and efficiency in reconstructing and identifying the oscillation signal.

The expected electron neutrino rates for full  $\nu_\mu \rightarrow \nu_e$  transmutation as a function of neutrino energy  $E_\nu$  are shown in Fig. 2.2, for both neutrino and antineutrino running modes. These distributions are weighted according to the oscillation probability formula in Eq. 2.4 to estimate the number of oscillation signal events for any (3+2) model prior to event reconstruction and particle identification. The sensitivity calculation takes into account the differences in event rates in antineutrino versus neutrino running modes (about a factor of four difference), and the “wrong-sign”, neutrino contribution to the overall event rate in antineutrino mode (a contribution of about 30%), which has the effect of washing out CP-violating asymmetries. The

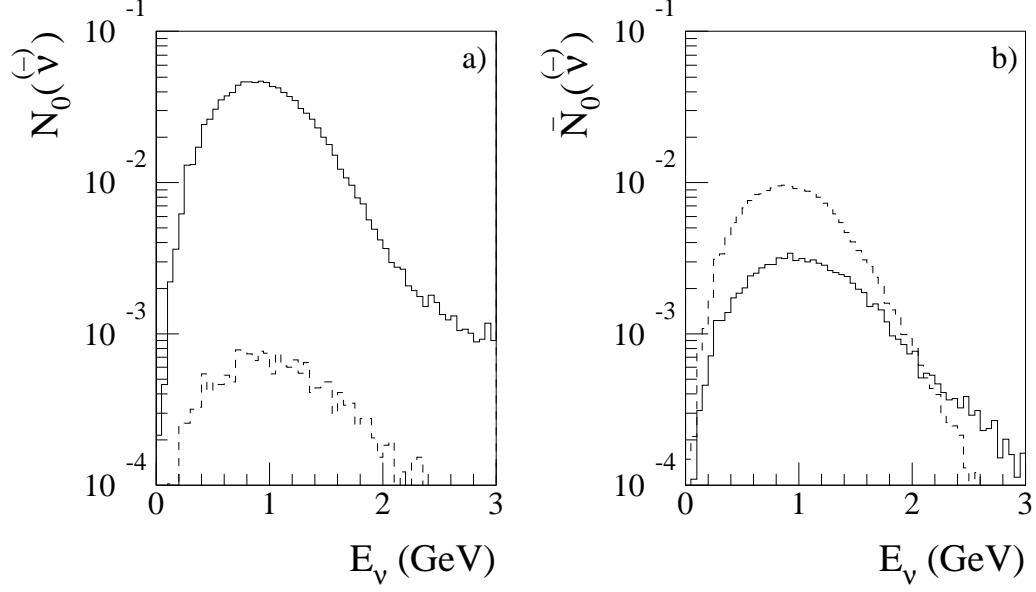


Figure 2.2: *Expected MiniBooNE electron neutrino rates for full  $\nu_\mu \rightarrow \nu_e$  transmutation as a function of neutrino energy  $E_\nu$ , in neutrino (panel a)) and antineutrino (panel b)) running modes. The solid histograms are for neutrinos, the dashed ones for antineutrinos. The histograms are normalized such that the overall rate in neutrino running mode is equal to one.*

MiniBooNE sensitivities for  $10^{21}$  protons on target presented in the following can be considered conservative, to the extent that they assume event counting only, and no fit to the shape of the neutrino energy distribution of the signal is performed.

### 2.3.3 Results

#### CP-conserving case

Figure 2.3 shows predictions for the oscillation signals to be expected in MiniBooNE neutrino and antineutrino modes, in the CP-conserving, (3+2) sterile neutrino model scenario. The MiniBooNE signal expectations are given in terms of the oscillation

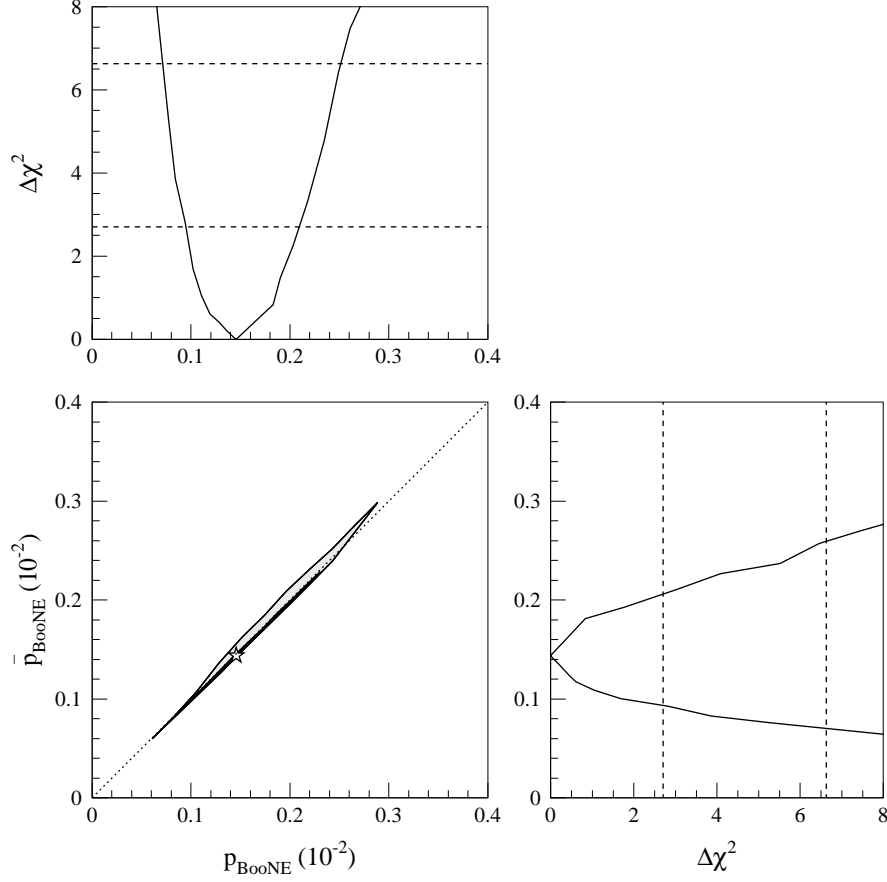


Figure 2.3: *Expected oscillation probabilities at MiniBooNE in neutrino and antineutrino running modes, for CP-conserving (3+2) models. See text for details.*

probability of Eq. 2.4, weighted by the full transmutation rates:

$$\bar{p}_{BooNE}^{(-)} = \frac{\int dE p(\nu_\mu \rightarrow \nu_e) [\bar{N}_0^{(-)}(\nu) + \bar{N}_0^{(-)}(\bar{\nu})]}{\int dE [\bar{N}_0^{(-)}(\nu) + \bar{N}_0^{(-)}(\bar{\nu})]} \quad (2.6)$$

where  $E$  is the neutrino energy,  $p(\nu_\mu \rightarrow \nu_e)$  is the oscillation probability of Eq. 2.4 in the CP-conserving case (*i.e.*,  $\phi_{54} = 0$  or  $\pi$ ),  $N_0(\nu)$  and  $N_0(\bar{\nu})$  are the neutrino and antineutrino full-transmutation rate distributions in neutrino running mode from Fig. 2.2a), and  $\bar{N}_0(\nu)$  and  $\bar{N}_0(\bar{\nu})$  are the neutrino and antineutrino full-transmutation rate distributions in antineutrino running mode from Fig. 2.2b).

The bottom left panel in Figure 2.3 shows the region in  $(p_{BooNE}, \bar{p}_{BooNE})$  space that is allowed at the 90% and 99% confidence level (2 dof) by existing short-baseline data used in the analysis, including LSND. The star indicates the best-fit, at

$p_{BooNE} \simeq \bar{p}_{BooNE} \simeq 0.14 \cdot 10^{-2}$ . We note here that the effect of “fake” CP-violation due to spectrum differences in neutrino and antineutrino running modes, which would manifest themselves as departures from the dotted line in the bottom left panel of Fig. 2.3, are at the few percent level at most.

The top left and bottom right panels in Fig. 2.3 show the 1-dimensional projections of the  $\chi^2$  contours obtained from existing short-baseline data, as a function of  $p_{BooNE}$  and  $\bar{p}_{BooNE}$ , respectively. The dashed lines at  $\Delta\chi^2=2.70$  and 6.63 indicate the 90% and 99% CL regions, respectively (1 dof). MiniBooNE is expected to measure an oscillation probability in excess of  $\simeq 0.07 \cdot 10^{-2}$  in the current neutrino running mode, if CP-conserving (3+2) models are correct.

Figure 2.4 is the same as Fig. 2.3, with the exception that the MiniBooNE sensitivities  $p_{BooNE}/\delta p_{BooNE}$  and  $\bar{p}_{BooNE}/\delta \bar{p}_{BooNE}$  are shown instead of the oscillation probabilities  $p_{BooNE}$  and  $\bar{p}_{BooNE}$ . As mentioned before, the  $1\sigma$  uncertainties  $\delta p_{BooNE}$  and  $\delta \bar{p}_{BooNE}$  associated with the measurement of the oscillation probabilities in neutrino and antineutrino running modes include both the statistical uncertainty of the oscillation signal prediction (for  $10^{21}$  protons on target), and the systematic uncertainty of the background prediction.

The bottom left panel in Fig. 2.4 shows that the antineutrino oscillation probability significance is always lower than the neutrino oscillation probability significance, for allowed, CP-conserving (3+2) sterile neutrino models, because of the inherent lower event statistics. Moreover, it is found that the most likely MiniBooNE oscillation significances in an event counting only analysis are about  $5\sigma$  in neutrino mode, and  $4\sigma$  in antineutrino running modes. we note here that these best-fit MiniBooNE oscillation significances are obtained by including several null short-baseline results in the analysis, which tend to reduce the magnitude of the LSND-only neutrino oscillation result.

The top left panel in Fig. 2.4 shows that the MiniBooNE 99% CL sensitivity (1 dof), defined as  $p_{BooNE}/\delta p_{BooNE} \equiv \sqrt{6.63} = 2.57$ , just covers all the neutrino mode



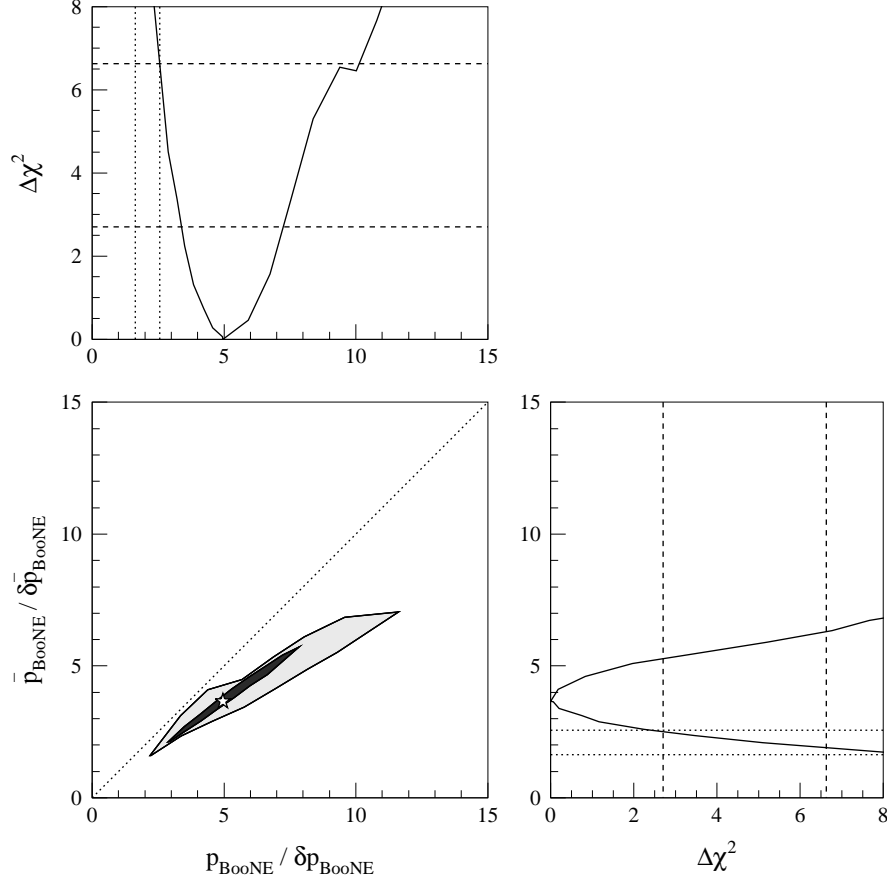


Figure 2.4: *Expected oscillation significances at MiniBooNE in neutrino and antineutrino running modes, for CP-conserving (3+2) models. See text for details.*

oscillation signals from CP-conserving, (3+2) models allowed at 99% CL (1 dof).

### CP-violating case

The same analysis methods and formalism presented above is now applied to CP-violating, (3+2) sterile neutrino models. In this case, the CP-violating phase  $\phi_{54}$  can assume any value between 0 and  $2\pi$ , and the neutrino and antineutrino oscillation probabilities  $p(\nu_\mu \rightarrow \nu_e)$  and  $p(\bar{\nu}_\mu \rightarrow \bar{\nu}_e)$  are generally different. Therefore, the oscillation probabilities in neutrino and antineutrino running modes, averaged over

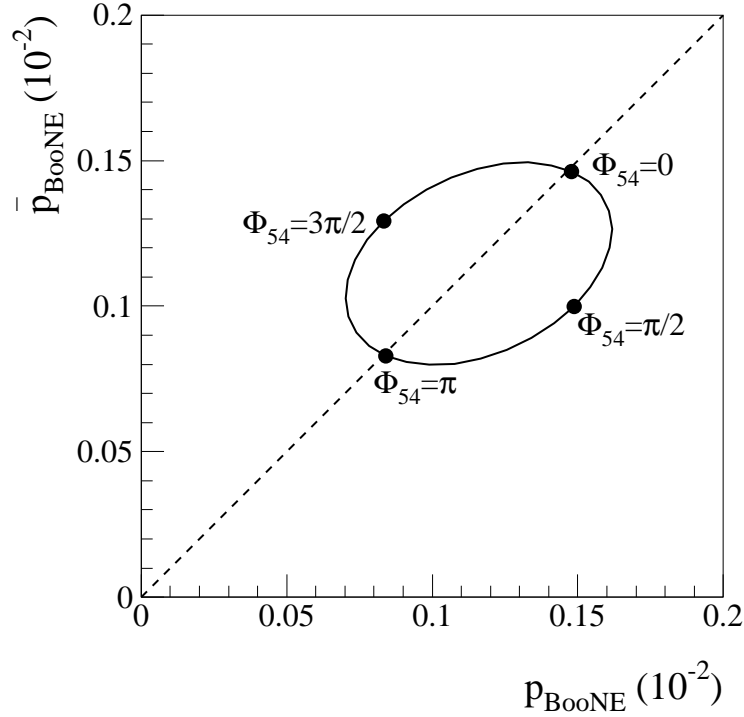


Figure 2.5: *Illustration of oscillation probabilities to be expected at MiniBooNE in neutrino and antineutrino running modes, for CP-violating, (3+2) sterile neutrino models. For this particular plot, neutrino masses and mixings are fixed to the values given in the text, while the CP-violating phase  $\phi_{54}$  is allowed to vary between 0 and  $2\pi$ .*

the MiniBooNE spectra, now read:

$$\bar{p}_{BooNE}^{(-)} = \frac{\int dE [p(\nu_\mu \rightarrow \nu_e) \bar{N}_0^{(-)}(\nu) + p(\bar{\nu}_\mu \rightarrow \bar{\nu}_e) \bar{N}_0^{(-)}(\bar{\nu})]}{\int dE [\bar{N}_0^{(-)}(\nu) + \bar{N}_0^{(-)}(\bar{\nu})]} \quad (2.7)$$

Figure 2.5 illustrates the order of magnitude of the CP-violating effects to be expected. In this plot, neutrino masses and mixings are fixed to their best-fit values of:  $\Delta m_{41}^2 = 0.92 \text{ eV}^2$ ,  $|U_{e4}| = 0.123$ ,  $|U_{\mu 4}| = 0.199$ ,  $\Delta m_{51}^2 = 21 \text{ eV}^2$ ,  $|U_{e5}| = 0.039$ ,  $|U_{\mu 5}| = 0.215$ , and the only parameter that is allowed to vary is the CP-violating phase  $\Phi_{54}$ . In this particular case, neutrino/antineutrino running mode oscillation probability differences as big as a factor of two can be obtained, near maximal CP-violation ( $\phi_{54} = \pi/2$  or  $3\pi/2$ ).

Figure 2.6 shows the oscillation probabilities to be expected at MiniBooNE in

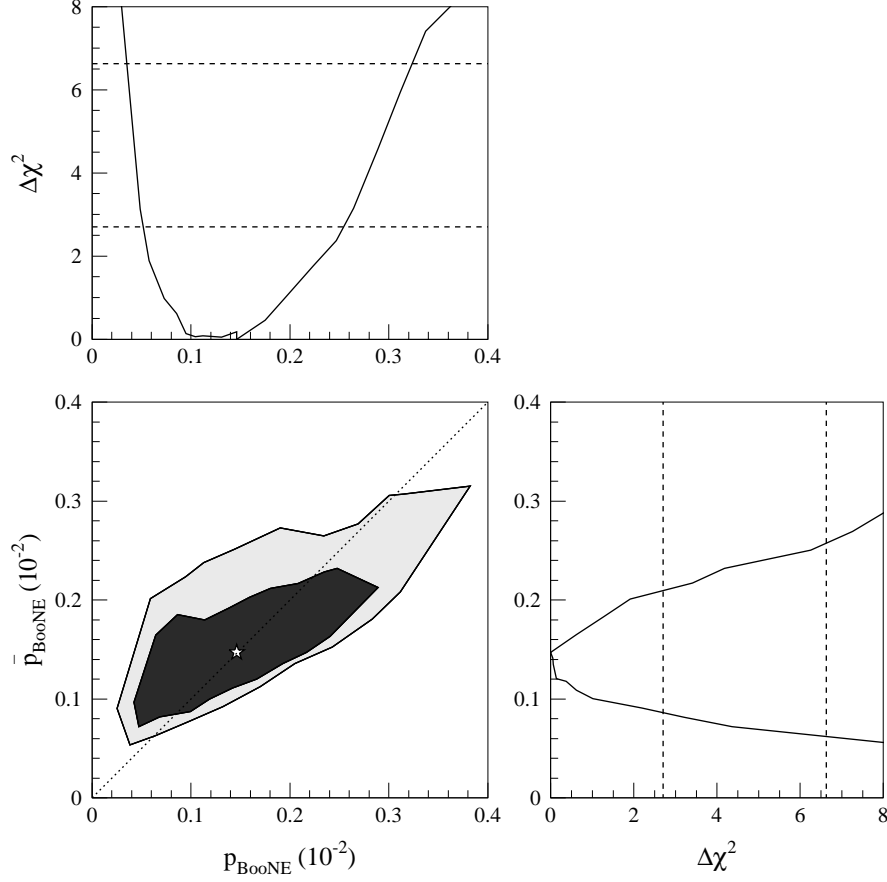


Figure 2.6: *Expected oscillation probabilities at MiniBooNE in neutrino and antineutrino running modes, for CP-violating (3+2) models.*

neutrino and antineutrino running modes, in a CP-violating, (3+2) scenario. Unlike Fig. 2.5, all parameters ( $\Delta m_{41}^2, |U_{e4}|, |U_{\mu 4}|, \Delta m_{51}^2, |U_{e5}|, |U_{\mu 5}|, \phi_{54}$ ) are now allowed to vary within the constraints provided by existing short-baseline oscillation results. Compared to the CP-conserving case of Fig. 2.3, the best-fit point (indicated by a star) does not change significantly; however, large asymmetries due to CP-violation are now possible, shown by departures from the dashed line in the bottom left panel of Fig. 2.6. The general trend is that the 2-dimensional allowed region in  $(p_{BooNE}, \bar{p}_{BooNE})$  space is tilted more horizontally compared to the dashed line  $\bar{p}_{BooNE} = p_{BooNE}$ , indicating that existing short-baseline results constrain more  $\bar{\nu}_\mu \rightarrow \bar{\nu}_e$  than  $\nu_\mu \rightarrow \nu_e$  oscillations.

In the CP-violating case, MiniBooNE is expected to measure an oscillation prob-

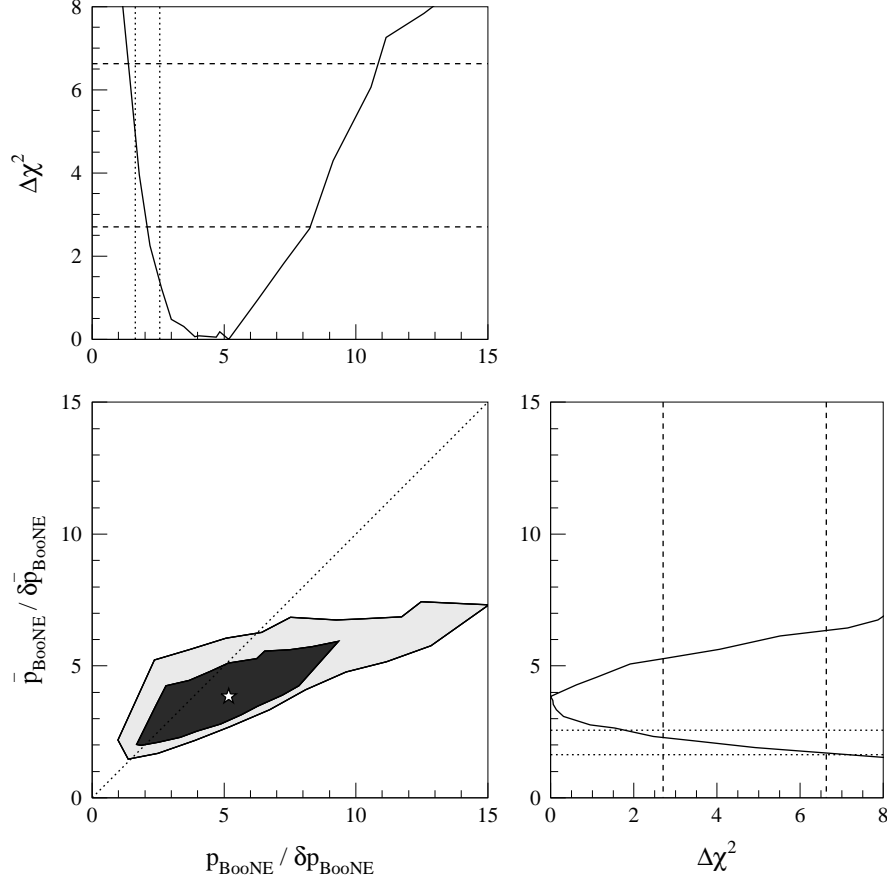


Figure 2.7: *Expected oscillation significances at MiniBooNE in neutrino and antineutrino running modes, for CP-violating (3+2) models.*

baility in excess of  $\simeq 0.04 \cdot 10^{-2}$  in the current neutrino running mode.

In Fig. 2.7, we show the expected MiniBooNE significances in neutrino and antineutrino running modes, for an oscillation signal in the CP-violating (3+2) scenario. If CP-violation is present, it is possible to have, for certain models, a higher oscillation probability significance in MiniBooNE antineutrino mode rather than in neutrino running mode. In particular, the MiniBooNE 90% CL sensitivity just covers the 99% CL (1 dof) allowed oscillation range in antineutrino mode, and a lower coverage is obtained in neutrino mode. Opposite effects are also possible, and significances of more than  $10 \sigma$  in neutrino mode could be observed at MiniBooNE in this case.

From this analysis, it is clear that a MiniBooNE antineutrino run would be highly desirable to fully address the LSND antineutrino oscillation signal indication.

Finally, we discuss what are the present constraints on the CP-phase  $\phi_{54}$  that are currently available from a CP-violating, (3+2) analysis of short-baseline data, and what is the MiniBooNE CP-asymmetry sensitivity for these allowed values. The CP-asymmetry is defined here as:

$$A_{CP} = \frac{p_{BooNE} - \bar{p}_{BooNE}}{p_{BooNE} + \bar{p}_{BooNE}} \quad (2.8)$$

The uncertainty on the MiniBooNE CP-asymmetry measurement,  $\delta A_{CP}$ , is obtained here by standard error propagation, assuming the  $\delta p_{BooNE}$  and  $\delta \bar{p}_{BooNE}$  uncertainties to be uncorrelated. This assumption should be reasonable, to the extent that the MiniBooNE measurements are statistics-dominated, and it represents a conservative assumption.

The top left panel in Fig. 2.8 shows that all values for the CP-phase  $\phi_{54}$  are presently allowed at the 99% confidence level, and that CP-violating, (3+2) models with small degrees of CP violation are marginally preferred.

The bottom left plot shows that large CP asymmetry significances are possible (but not required) for maximal CP-violation, given by phases of about  $\Phi_{54} = \pi/2$  and  $3\pi/2$ . The dotted lines in the bottom right panel indicate the MiniBooNE 90% and 99% CL sensitivity lines to a CP-violating asymmetry, defined as  $A_{CP}/\delta A_{CP} = \sqrt{2.70} = 1.64$  and  $\sqrt{6.63} = 2.57$ , respectively. The bottom left and right plots indicate that a measurement of CP asymmetry at MiniBooNE with more than  $3\sigma$  significance is possible under favorable circumstances, for CP-violating (3+2) models currently allowed at the 99% confidence level, even though no significant CP asymmetry would be observed at MiniBooNE in the most likely (3+2) scenarios.

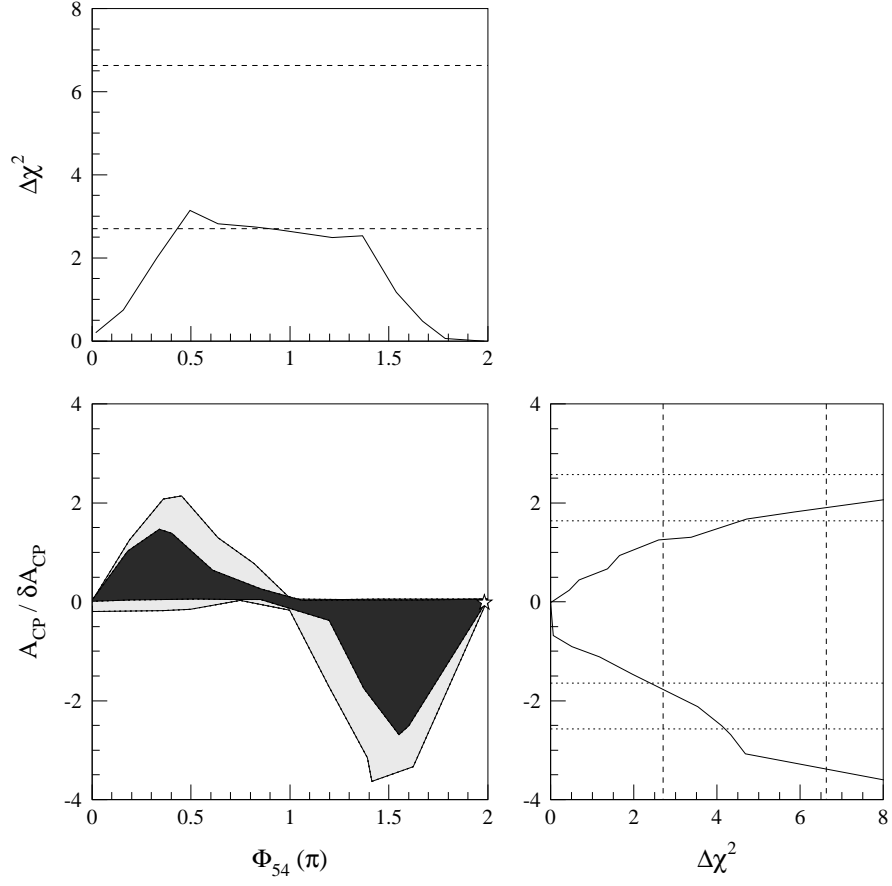


Figure 2.8: *Current limits on the CP-violating phase  $\phi_{54}$  from current short-baseline results, and significance of a CP asymmetry measurement expected at MiniBooNE,  $A_{CP}/\delta A_{CP}$ .*

# Bibliography

- [1] M. Sorel and J. M. Conrad, Phys. Rev. D **66**, 033009 (2002) [arXiv:hep-ph/0112214].
- [2] M. Sorel, J. M. Conrad and M. Shaevitz, Phys. Rev. D **70**, 073004 (2004) [arXiv:hep-ph/0305255].
- [3] A. Aguilar-Arevalo, V. Barger, J. M. Conrad, M. Shaevitz, M. Sorel, K. Whisnant, “CP violation in (3+2) sterile neutrino models,” in preparation.
- [4] P. Brâemaud, *Markov chains: Gibbs fields, Monte Carlo simulation, and queues*, Springer, New York, 1999.
- [5] N. Metropolis, A. W. Rosenbluth, M. N. Rosenbluth, A. H. Teller and E. Teller, J. Chem. Phys. **21**, 1087 (1953).
- [6] <http://www-boone.fnal.gov/publicpages/runplan.ps.gz>